

REPORT

# *Rickettsia parkeri* forms extensive, stable contacts with the rough endoplasmic reticulum

Yamilex Acevedo-Sánchez<sup>1</sup>, Patrick J. Woida<sup>1</sup>, Caroline Anderson<sup>1,2</sup>, Stephan Kraemer<sup>3</sup>, and Rebecca L. Lamason<sup>1,2</sup>

Upon invasion into the host cell, a subset of bacterial pathogens resides exclusively in the cytosol. While previous research revealed how they reshape the plasma membrane during invasion, subvert the immune response, and hijack cytoskeletal dynamics to promote their motility, it was unclear if these pathogens also interacted with the organelles in this crowded intracellular space. Here, we examined if the obligate intracellular pathogen *Rickettsia parkeri* interacts with the endoplasmic reticulum (ER), a large and dynamic organelle spread throughout the cell. Using live-cell microscopy and transmission and focused-ion-beam scanning electron microscopy, we show that *R. parkeri* forms extensive contacts with the rough ER that are ~55 nm apart and cover more than half the bacterial surface. Depletion of the ER-specific tethers VAPA and VAPB reduced rickettsia-ER contacts, and VAPA and VAPB were localized around intracellular rickettsiae. Overall, our findings illuminate an interkingdom ER contact uniquely mediated by rickettsiae that mimics some characteristics of traditional host membrane contact sites.

## Introduction

Several human pathogens live freely inside the host cytosol, including the tick-borne bacterium *Rickettsia parkeri*, which causes a mild spotted fever disease in humans (Walker and Ismail, 2008; Sit and Lamason, 2024). Similar to other intracellular bacteria like *Listeria monocytogenes* and *Shigella flexneri*, *R. parkeri* invades host cells, escapes to the cytosol, hijacks the actin cytoskeleton to move intracellularly, and then disseminates through our tissues using a process known as cell-to-cell spread (Lamason and Welch, 2017; Raab et al., 2024). Unlike *L. monocytogenes* and *S. flexneri*, though, *Rickettsia* species are obligate intracellular pathogens entirely dependent on their host cell for survival. Consequently, this dependency has led to unique adaptations, including unexpected mimicry of host cell biology (Lamason and Welch, 2017; McGinn and Lamason, 2021).

In uninfected settings, eukaryotic organelles do not exist in isolation and can interact through various forms of dynamic or stable interactions. Indeed, the largest organelle, the endoplasmic reticulum (ER), acts as a major cellular scaffold bridging multiple organelles to itself through interorganelle contacts (Prinz et al., 2020; Wu et al., 2018). Contact sites with the smooth ER span 10–30 nm, while interactions with the rough ER can reach up to 80-nm wide (Giacomello and Pellegrini, 2016; Scorrano et al., 2019). Their cellular functions are diverse, impacting lipid metabolism and transport, organelle dynamics and function, calcium transfer, autophagy, and apoptosis (Phillips

and Voeltz, 2016). Many contacts also rely on a cadre of protein tethers. The most well-characterized of which are the vesicle-associated membrane protein-associated protein-A and -B (VAPA and VAPB) (Costello et al., 2017; Alpy et al., 2013; De Vos et al., 2012; Lehto et al., 2005; Rocha et al., 2009; Wyles et al., 2002), and recent evidence suggests these are vulnerable to intracellular pathogen manipulation. For example, infection with  $\beta$ -herpesvirus human cytomegalovirus increases VAPA and VAPB expression to impact the dynamics of ER-mediated membrane contact sites (MCS) with other organelles (Cook et al., 2022). In contrast, the pathogenic bacterium *Chlamydia trachomatis* hijacks VAPA and VAPB to connect its host-derived vacuolar compartment to the ER (Derré et al., 2011; Stanhope et al., 2017). These examples demonstrate the diversity of mechanisms pathogens have evolved to subvert these eukaryotic membrane interfaces, suggesting a critical role for MCS in host-pathogen interactions. However, it is unclear if cytosolic bacterial pathogens like *R. parkeri* can similarly interact with eukaryotic organelles.

Here, we used a combination of imaging modalities to investigate if *R. parkeri* interacted with the ER. We discovered that a subset of *R. parkeri* makes stable, close contacts with the rough ER (RER), but *L. monocytogenes* or *S. flexneri* never formed these same structures. The frequency of these RER contacts also dramatically increased for a mutant *R. parkeri* strain that cannot

<sup>1</sup>Department of Biology, Massachusetts Institute of Technology, Cambridge, MA, USA; <sup>2</sup>Microbiology Program, Massachusetts Institute of Technology, Cambridge, MA, USA; <sup>3</sup>Center for Nanoscale Systems, Harvard University, Cambridge, MA, USA.

Correspondence to Rebecca L. Lamason: [rlamason@mit.edu](mailto:rlamason@mit.edu).

© 2025 Acevedo-Sánchez et al. This article is distributed under the terms as described at <https://rupress.org/pages/terms102024/>.

undergo actin-based motility. Interactions with the RER and rickettsiae were extensive and typically enveloped more than half of the surface of *R. parkeri*. We further provide evidence that VAPA and VAPB are recruited to *R. parkeri* and are required for the bacteria-ER contacts, suggesting that an unknown VAP target mediates this novel interkingdom contact between the RER and rickettsiae.

## Results and discussion

### *R. parkeri* forms stable interactions with the ER

To identify putative interactions between the ER and *R. parkeri*, we infected A549 cells stably expressing a fluorescent ER marker (mCherry-Sec61 $\beta$ ) (Zurek et al., 2011) with TagBFP-expressing *R. parkeri* (RpBFP). Using live-cell imaging, we found that 3–4% of RpBFP colocalized with the ER at 28 and 48 h post-infection (hpi), and these interactions were subdivided into two distinctive patterns: vacuole-like and protrusive ER structures (Fig. 1, A–C). Protrusive ER structures were found extending into the nucleus or through the cytoplasm (Fig. 1 B). Vacuole-like ER structures around bacteria were only found in the cytoplasm (Fig. 1 B). These colocalization patterns were independent of the fluorescent ER marker used, as we obtained similar results with another ER marker (BiP-mNeon-Green-KDEL) (Fig. S1 A) (Friedman et al., 2011). The interactions also appeared to be specific to *R. parkeri* because no interactions were seen with the ER during infection with *L. monocytogenes* or *S. flexneri* (Fig. S1, B and C).

A subpopulation of *R. parkeri* polymerizes an actin tail (Haglund et al., 2010; Reed et al., 2014), and ER protrusions may form from motile *R. parkeri* running into the ER. To investigate this hypothesis, we labeled A549-BiP-mNeonGreen-KDEL cells with the filamentous actin (F-actin) probe SIR-actin (Lukinavičius et al., 2014) and found that most protrusive structures are associated with actin, whereas none of the vacuole-like ER structures had actin tails (Fig. 1, D and E). These results suggest that ER protrusive structures are formed by actin-propelled bacteria interacting with the ER.

We next investigated the vacuole-like ER structures, which appeared more stably associated with bacteria than the protrusive structures (Fig. 1 B). In uninfected settings, ER interactions with other organelles are either short-lived, lasting several seconds (Friedman et al., 2011; Guo et al., 2018; Rowland et al., 2014), or more stable, lasting several minutes (Lee et al., 2020; Valm et al., 2017). Using live-cell imaging, we quantified the duration of the vacuole-like ER interactions around bacteria over a 3-min period and observed over 90% of the vacuole-like ER structures persisted for >2 min, despite the highly dynamic nature of the ER (Fig. 1 F and Video 1). More significant stability was also observed, with a fraction of these structures persisting over our extended, hour-long imaging sessions (Fig. 1 G). Occasionally, we also observed these interactions spontaneously form around a bacterium in the cytoplasm (Video 2). These data demonstrate that non-motile *R. parkeri* form stable interactions with the ER.

### Immobile bacteria display increased interactions with the ER

The stability and lack of actin tails associated with the vacuole-like ER structures prompted us to speculate that an *R. parkeri*

mutant that cannot hijack the actin cytoskeleton would form more vacuole-like ER structures relative to WT *R. parkeri*. To test this, we used a mutant with a transposon insertion in *sca2*, a rickettsial gene that encodes a human formin mimic protein required for bacterial actin-based motility (Kleba et al., 2010; Reed et al., 2014; Haglund et al., 2010), and compared it to WT (RpBFP) using live-cell imaging. We observed that the frequency of *sca2*::Tn mutant bacteria interacting with the ER was nearly 25-fold higher than WT (Fig. 2 A). Additionally, the *sca2*::Tn mutant completely lacked any protrusive structures (Fig. 2 B), supporting our earlier conclusion that ER protrusions result from actin-propelled *R. parkeri*. Finally, these interactions were not observed with mutants of *L. monocytogenes* ( $\Delta$ actA) and *S. flexneri* (*icsA*:: $\Omega$ ) also impaired in actin-based motility (Bernardini et al., 1989; Domann et al., 1992; Kocks et al., 1992; Makino et al., 1986) (Fig. S1, B and C). Together, these data show that a lack of actin-based motility increases the incidence of the unique interactions between rickettsiae and the ER.

The interactions between the ER and *sca2*::Tn mutant bacteria were also extremely stable, with >90% of the bacteria stably associated with the ER for the entire hour of imaging (Fig. 2 C and Video 3). We also observed that  $39 \pm 8.1\%$  (SEM;  $n > 50$  cells from three independent experiments) of host cells displayed nearly uniform interactions between the *sca2*::Tn mutant and the ER, while other host cells were devoid of these interactions (Fig. 2 D). The bimodal nature of these interactions was not correlated with differences in intracellular bacterial burdens because cells that had these rickettsia-ER structures had similar bacterial loads to cells that lacked these structures (Fig. 2 E). Additionally, we could often see bacteria with septa wrapped by the ER, showcasing they are capable of replicating. Next, we considered if these structures were associated with autophagy. The *sca2*::Tn mutant was previously shown not to localize with ubiquitin (Engström et al., 2019), and we did not observe colocalization with p62 at timepoints showing rickettsia-ER structures (Fig. S2, A and B). The frequency of interactions between *sca2*::Tn mutant bacteria and the ER also remained unchanged in HeLa cells lacking the key autophagy protein ATG5 (Nezich et al., 2015) (Fig. S2C, D). Moreover, an *ompB*::Tn mutant targeted by autophagy (Engström et al., 2019; Lamason et al., 2018) forms rickettsia-ER structures at similar frequencies to WT rickettsiae (Fig. S2, E and F). These observations suggest that rickettsia-ER structures do not grossly impact bacterial replication and are distinct from rickettsial interactions with autophagosomal membranes. Consequently, the *sca2*::Tn mutant strain emerged as a valuable model for further dissection of the rickettsia-ER interactions.

### *R. parkeri* is partially wrapped by the rough ER in different cell types

Stable interactions with the ER could occur by rickettsiae gaining access to the ER lumen or from cytosolic bacteria being wrapped by the ER network. To differentiate between these possibilities, we used transmission electron microscopy (TEM) to resolve the rickettsia-ER interactions in A549 cells infected with the *sca2*::Tn mutant. We did not detect rickettsiae inside the lumen of single-membrane structures. Instead, bacteria were partially wrapped by

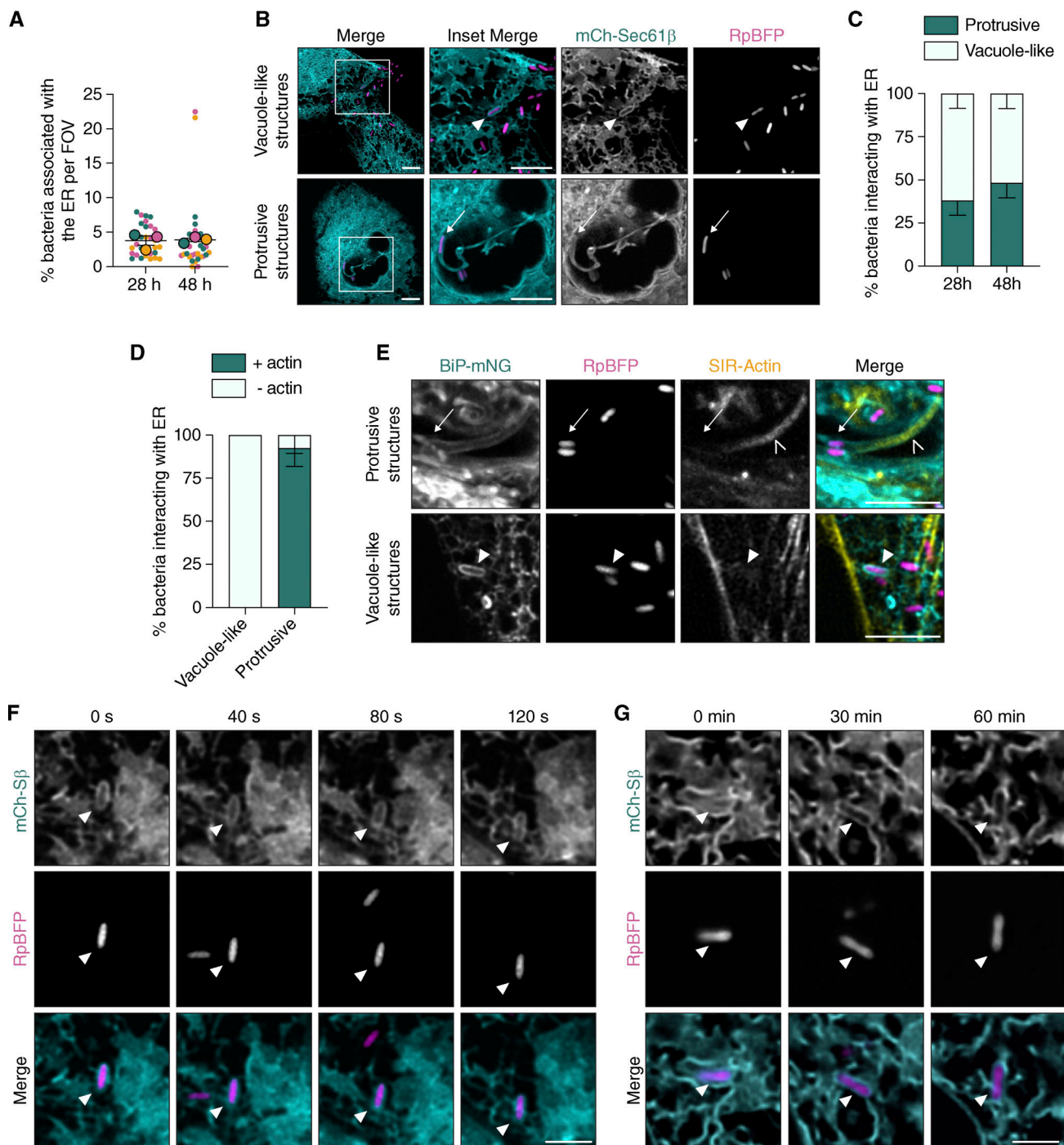
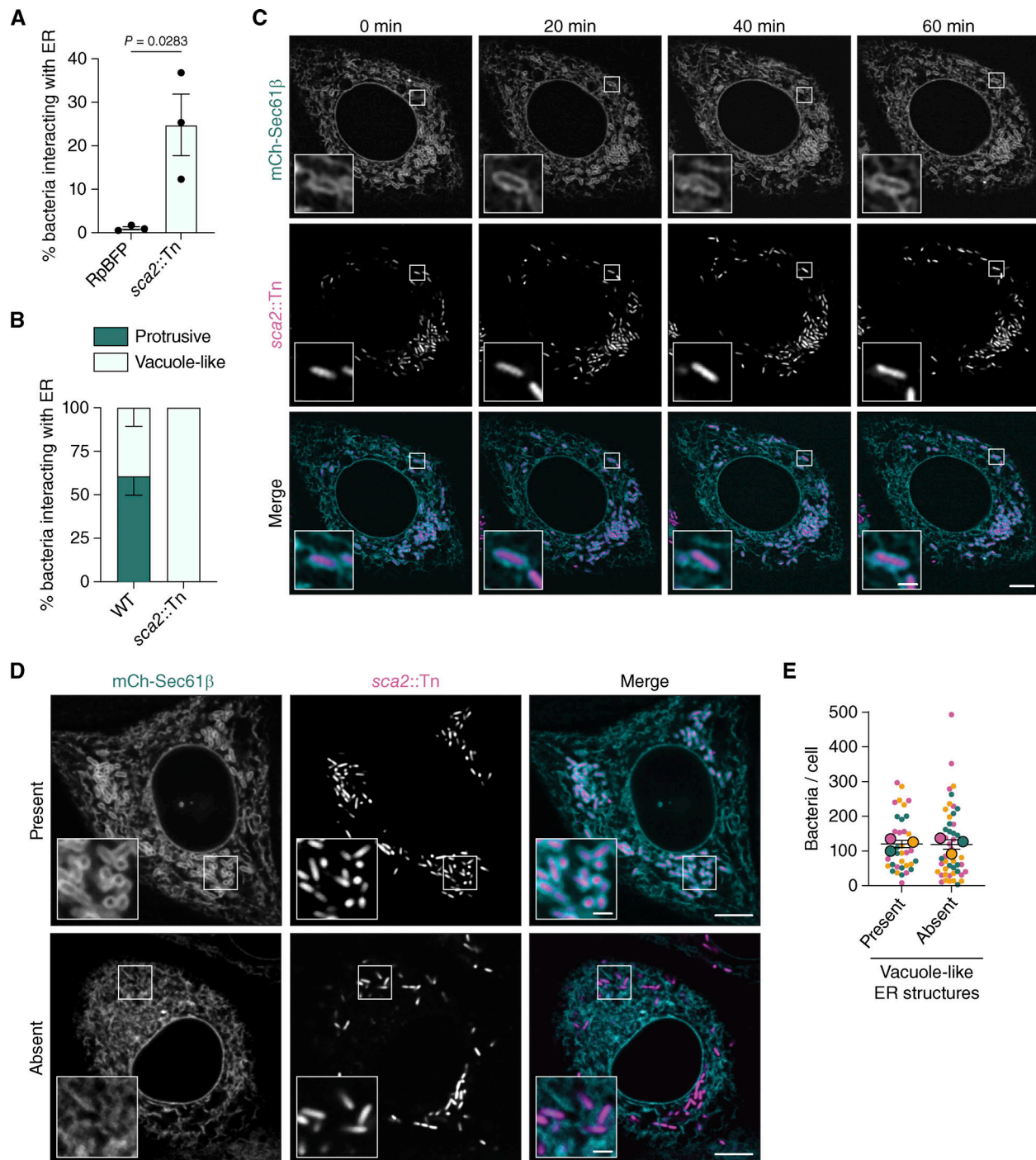
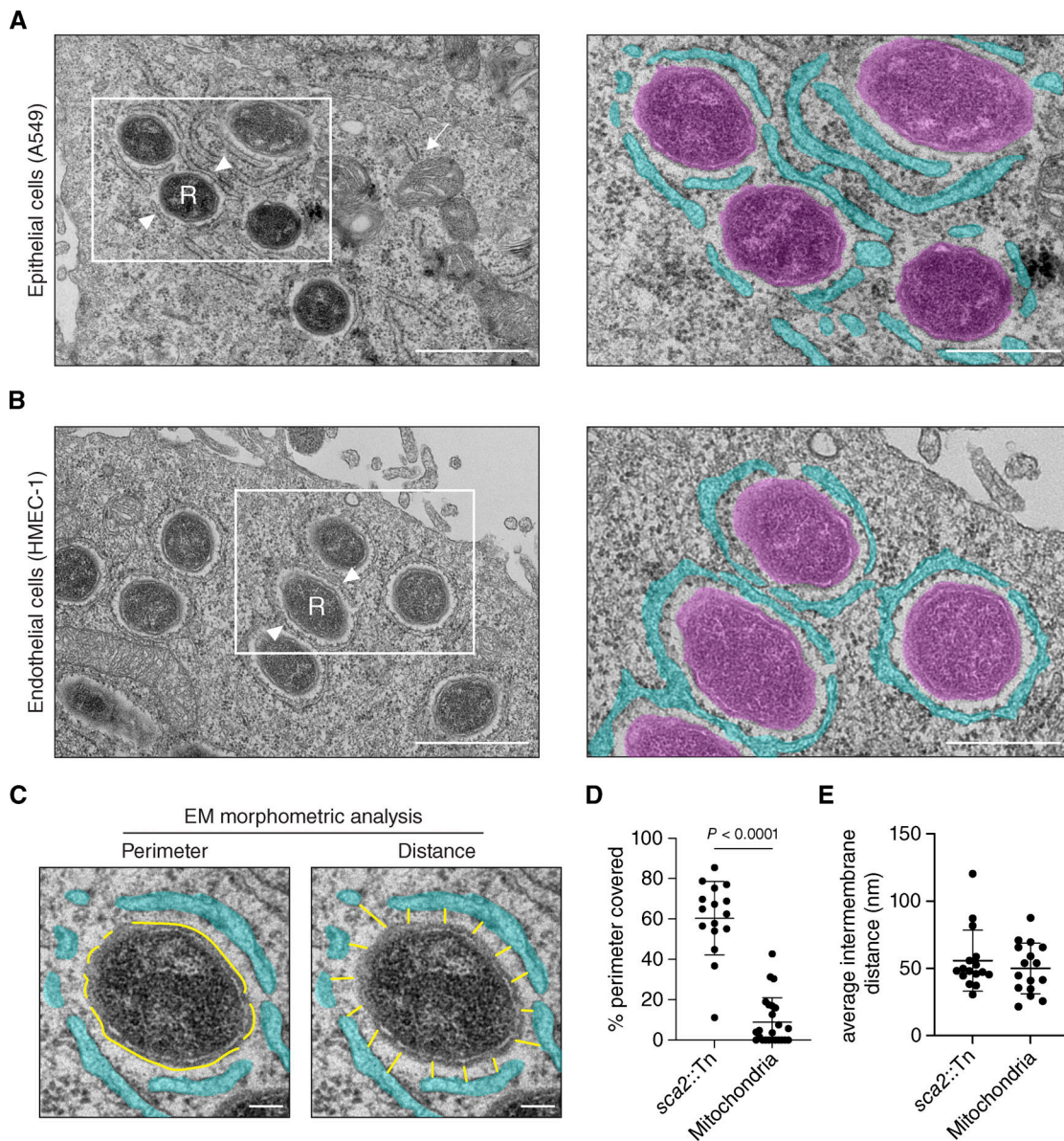


Figure 1. *R. parkeri* interacts with the ER. (A) Percentage of bacteria interacting with the ER structures in B. The mean  $\pm$  SEM of three independent experiments (large outlined circles) is superimposed over the raw data (small unlined circles) representing the percentage per FOV (>2,000 bacteria counted per independent experiment, data are colored by experiment). (B) Live-cell imaging snapshots at 28 hpi of WT *R. parkeri* (magenta, RpBFP) in vacuole-like (arrowhead) or protrusive (arrow) ER structures (cyan, mCherry-Sec61β). Scale bar, 5 μm; inset, 2.5 μm. (C) Relative frequency of bacteria interacting with the ER in B that are forming protrusive or vacuole-like structures at 28 or 48 hpi. Error bars indicate SEM from three independent experiments (>80 bacteria counted per independent experiment). (D) Relative frequency of bacteria interacting with the ER that display an actin tail at 48 hpi (as in E). Data presented are mean  $\pm$  SD. Approximately 10 FOVs were imaged per strain for each replicate ( $n = 2$ ) and >100 bacteria interacting with the ER were quantified. (E) From part D, live-cell imaging snapshots at 48 hpi of SIR-actin (yellow, open arrowhead) and RpBFP (magenta) in vacuole-like (arrowhead) or protrusive (arrow) ER structures (cyan, BiP-mNeonGreen-KDEL). Scale bar, 5 μm. (F and G) Live-cell imaging snapshots of vacuole-like rickettsia-ER structures (arrowhead) over time. Scale bar, 2.5 μm. Seconds, s; minutes, min.



**Figure 2. The *sca2::Tn* mutant displays increased interactions with the ER.** (A) Percentage of RpBFP or *sca2::Tn* mutant bacteria forming vacuole-like ER structures at 48 hpi. RpBFP data are independent of that shown in Fig. 1. Each dot represents the mean percentage of bacteria interacting with the ER for three independent experiments (>4,000 bacteria per independent experiment). Error bars represent SEM (unpaired two-tailed *t* test). (B) Relative frequency of RpBFP or *sca2::Tn* mutant bacteria forming protrusive or vacuole-like ER structures at 48 hpi. Error bars indicate SEM from three independent experiments (>100 bacteria counted per independent experiment). (C) Live-cell imaging snapshots at 48 hpi of *sca2::Tn* mutant bacteria (magenta) infecting A549-mCherry-Sec61β cells (cyan). Scale bar, 5 μm; inset, 1 μm. (D) Live-cell imaging snapshots as in C showing cells with (present) or without (absent) vacuole-like ER structures at 48 hpi. Scale bar, 5 μm; inset, 1 μm. (E) Number of bacteria in cells at 48 hpi with vacuole-like ER structures present or absent (images in D). The mean ± SEM of three independent experiments (large outlined circles) are superimposed over the raw data from individual cells (small unlined circles) (>10 cells counted per independent experiment, data are colored by experiment).



**Figure 3. *R. parkeri* is partially wrapped by the rough ER in different cell types.** (A and B) TEM images at 30 hpi of A549 (A) and HMEC-1 (B) cells infected with *sca2::Tn* mutant bacteria. R, rickettsia (arrowhead), RER-wrapped bacterium (arrow), mitochondria–RER interaction. Insets—bacteria (magenta) and ER (cyan). Scale bar, 1  $\mu$ m; inset, 500 nm. (C) 2D morphometric analysis examples are used to quantify the average bacterial perimeter covered by the RER (left) or the average distance between RER and bacterial membranes (right) (from cells in A). ER, cyan; yellow lines represent traces measured. (D and E) Percentage of the bacterial or mitochondrial perimeter covered by the RER and the average distance between the membranes. Each dot represents an individual bacterium or mitochondrion (>10 counted). Each dot represents an individual bacterium or mitochondrion. Data shown are mean  $\pm$  SD from an independent replicate (unpaired two-tailed *t* test).

double membranes that contained ribosomes, indicating that the RER network specifically wrapped around cytosolic bacteria (Fig. 3 A). We additionally observed similar RER-specific structures in infected human microvascular endothelial cells (HMEC-1) (Fig. 3 B), a physiologically relevant target of *Rickettsia* species (Bradford et al., 1979; Kim et al., 2004; Roggli et al., 1985). Thus, the rickettsia–RER interaction is conserved in distinct cell types.

***R. parkeri* forms extensive interkingdom contacts with the RER**  
The ER interacts with mitochondria and other organelles to form MCS that regulate a variety of cell processes (Scorrano et al.,

2019; Prinz et al., 2020; Voeltz et al., 2024). Partial wrapping of the RER around rickettsiae is akin to recent observations of RER wrapping around mitochondria in liver cells (Hung et al., 2017; Anastasia et al., 2021), prompting us to examine if they had shared features to mitochondrial–ER MCS. Mitochondria–RER contacts are often 25–80 nm apart (Anastasia et al., 2021; Wang et al., 2015; Parlakgöl et al., 2024) with a large fraction of the mitochondria perimeter wrapped by the RER (Dai et al., 2005; Giacomello and Pellegrini, 2016; Rizzuto et al., 1998; Vance, 1990; Parlakgöl et al., 2024). Using 2D-morphometric analysis of our TEM data, we observed that ~58.7% of the bacterial perimeter

was surrounded by the RER (Fig. 3, C and D) maintaining consistent intermembrane distances. The extent of this interaction appeared to be specific because nearby mitochondria only showed interactions with the RER across ~8.4% of their perimeter (Fig. 3, C and D). We next measured the average distance between the RER membrane and the bacterial or mitochondrial surface along the perimeter of the contacts. We found that the RER had comparable average distances of ~55.7 and 50 nm to the rickettsial and mitochondrial surfaces, respectively (Fig. 3, C and E). Importantly, these distances match those reported for mitochondria–RER contacts under chemical-fixation conditions (Parlakgöl et al., 2024). Consequently, we have named these bacterium–ER contacts, or BERCs, for the ability of rickettsiae to form interkingdom contacts with the ER.

We next used focus ion beam electron microscopy (FIB–SEM) to capture a greater extent of the rickettsial surface and attain a 3D view of BERCs. Using deep learning segmentation, we generated 3D models of the rickettsia–ER structures during infection (Fig. 4 A and Video 4). These models confirmed our TEM data showing that >50% of the rickettsial surface is covered by the ER and showed that BERCs are connected to the greater ER network (Fig. 4 A and Video 5). We also observed regions of high-electron density connecting the ER to the bacterial membrane (Fig. 4 B). These structures exist throughout the rickettsia–ER interface and were present in all bacteria interacting with the ER.

#### VAPA and VAPB associate with *R. parkeri* and are required for BERC formation

The stability and consistent spacing of BERCs suggested that tethering proteins promote BERC formation. VAMP-associated proteins (VAPs) are ER-specific tethers that link the ER to different organelles, including the mitochondria, and are a common target for pathogen-mediated ER subversion (Vormittag et al., 2023; Paul and Tiwari, 2023). We occasionally observed that endogenous VAPA and VAPB localized around  $0.5 \pm 0.05\%$  and  $0.6 \pm 0.1\%$  of WT bacteria, respectively (SD from three independent experiments). As expected, a much higher frequency of colocalization was apparent with the *sca2::Tn* mutant (Fig. 5, A and B), with  $7 \pm 3\%$  and  $9 \pm 0.6\%$  of bacteria colocalizing with VAPA and VAPB, respectively (SD from three independent experiments). To determine if VAPs were required for BERC formation, we used RNA interference to deplete VAPA and VAPB in A549 cells (Fig. 5 C) and quantified BERC frequency using live-cell imaging. Knockdown of VAPA or VAPB expression led to a partial but significant decrease in the frequency of host cells containing BERCs, while simultaneous knockdown further reduced this frequency (Fig. 5 D). The frequency of BERCs was also nearly abolished in a previously published VAPA and VAPB double knockout (DKO) HeLa cell line (Dong et al., 2016), relative to WT HeLa cells (Fig. 5, E and F). Loss of VAPs was also not correlated with apparent differences in intracellular bacterial burdens (Fig. S3, A and B), in agreement with our data that BERCs do not grossly impact fitness (Fig. 2 E).

VAP recruitment to contacts requires recognition of two phenylalanines in an acidic tract (FFAT) and FFAT-like motifs in their protein binding partners (Alpy et al., 2013; Loewen et al., 2003; Di Mattia et al., 2020). Though the BERC-specific

target is unknown at this time, we hypothesized that the localization of VAPs to *R. parkeri* also required recognition of an FFAT-like motif. Previous work showed that overexpressed VAP proteins are found throughout the ER and are not enriched at most ER contact sites (Alpy et al., 2013; Dong et al., 2016; Barman et al., 2022; Obara et al., 2024), and we also were unable to detect enrichment of HaloTag fusions of full-length VAP proteins to BERCs (Fig. S3, C and D). Therefore, we sought a tool that would eliminate ER targeting while still maintaining the needed VAP multimerization for FFAT binding (Nishimura et al., 1999; Kim et al., 2010). We removed the VAP transmembrane domain and fused the remaining Halo–VAP $\Delta$ TM protein to the self-oligomerizing tag I3–01 (Hsia et al., 2016). Using these fusions, we detected robust localization of Halo–VAPA $\Delta$ TM–I3–01 and Halo–VAPB $\Delta$ TM–I3–01 around 24% and 42% of *sca2::Tn* mutant bacteria, respectively (Fig. 5, G and H). This localization was also largely bimodal, similar to what we observed for BERCs. Importantly, mutations in residues that mediate FFAT-binding in VAPA and VAPB (Kaiser et al., 2005) inhibited these interactions (see KD/MD fusions; Fig. 5, G and H). Together, these data indicate that VAPA and VAPB associate with the bacterium in a manner dependent on an FFAT-motif-containing protein.

#### Concluding remarks

The increased appreciation of interorganelle interactions in recent years has unveiled a set of closely apposed and tethered membranes that facilitate numerous cellular processes, making them prime candidates for microbial control or mimicry (Kors et al., 2022; Vormittag et al., 2023). Thus far, examples of pathogenic manipulation of ER-mediated interactions have been limited to contact sites between eukaryotic membrane compartments (Cook et al., 2022; Derré et al., 2011; Stanhope et al., 2017). Here, we report an example of a cytosolic bacterial pathogen forming an extensive, stable interkingdom contact with the RER during infection. We refer to these as BERCs and propose that these contacts rely on VAPA and VAPB binding partners.

Most contacts studied between the ER and other organelles involve the smooth ER. However, recent work has observed extensive wrapping of the RER around mitochondria in structures called riboMERCs (ribosome-studded Mitochondria–ER contacts) and wrapper (curved wrapping-type of RER) (Hung et al., 2017; Anastasia et al., 2021; Wang et al., 2015; Cardoen et al., 2024). It is curious that rickettsiae, whose evolutionary origins are linked with mitochondria (Sit and Lamason, 2024), also form extensive and stable interactions with the RER. Whether BERCs mimic the functional consequences of mitochondrial–ER contact sites or are distinct structures that perform their own unique function remains to be determined. Identification of all the molecular players key to forming BERCs will be needed to facilitate their functional dissection during infection.

Previous work has reported ER membranes near *Rickettsia conorii*, but these were attributed to autophagy and distinct from BERCs (Walker et al., 1997). ER dilation has also been observed during *R. rickettsii* infection, with the enlarged ER occasionally ramming into nearby organelles and bacteria (Silverman and Wisseman, 1979). Our observations were made well before

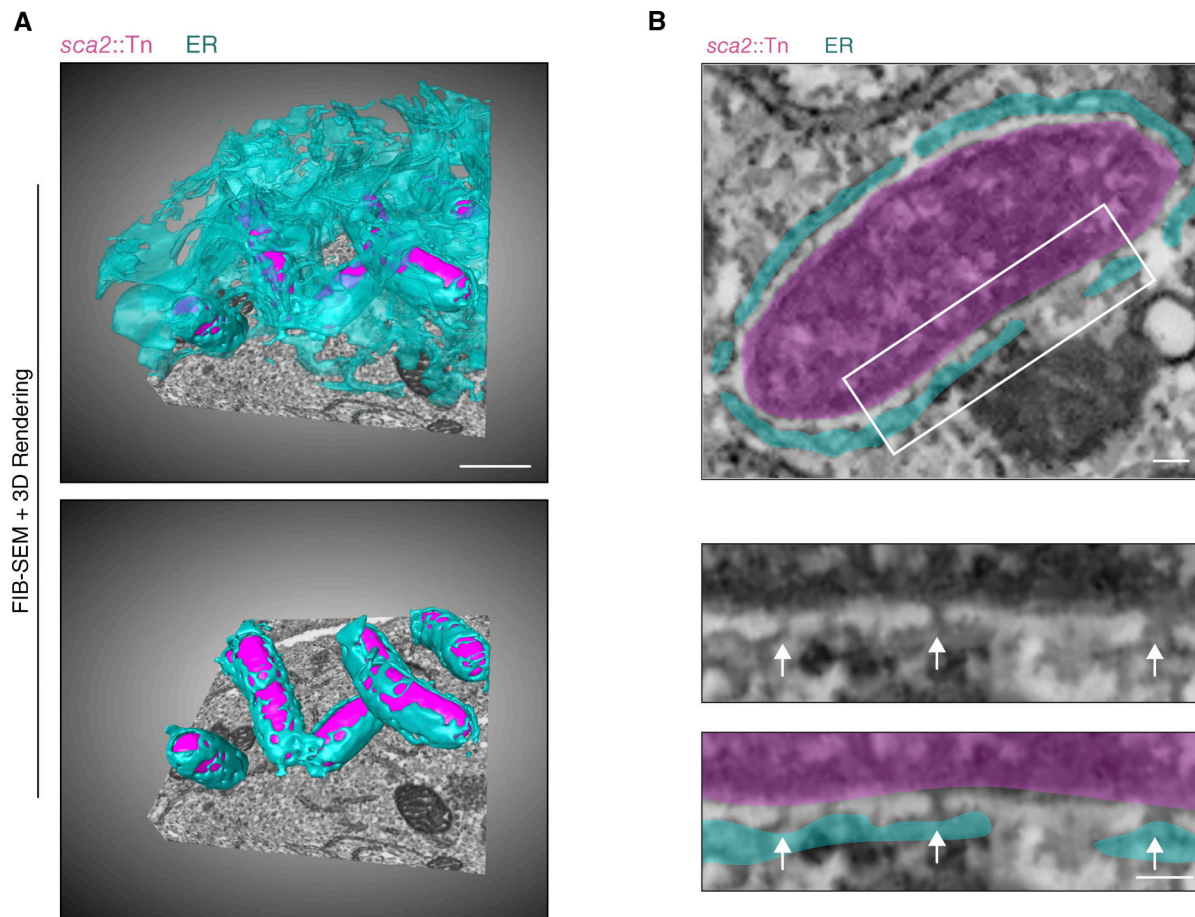


Figure 4. **Extensive interactions between *R. parkeri* and the RER network.** (A) FIB-SEM image stacks and 3D rendering of ER-rickettsia structures in A549 cells infected with the *sca2::Tn* mutant (magenta) at 30 hpi. The top image shows a subvolume of the FIB-SEM image stack acquired with the entire ER network (cyan) and the *sca2::Tn* mutant displayed. The bottom image only shows 3D rendering of the ER membranes adjacent to the bacterial membranes. Scale bar, 1  $\mu$ m. (B) FIB-SEM slice of a *sca2::Tn* mutant bacterium (magenta) from A. Insets at right show electron-dense regions (arrow) connecting the rickettsial (magenta) and ER (cyan) membranes. Scale bar, 100 nm.

obvious changes to the ER occurred, suggesting that these are separate phenomena. Intriguingly, a single example of the RER partially surrounding rickettsiae when inside tick cells was reported (Munderloh et al., 1998), but this report did not determine the nature of this interaction, and it is unknown if these structures match the BERCs we observed. Additional comparative studies between *Rickettsia* species and eukaryotic cell environments are needed.

BERCs were observed for only 3–4% of WT rickettsiae at the infection stages tested in this report. To what extent this frequency changes at different stages or under different cellular conditions remains to be determined. Importantly, though, heterogeneity within the intracellular rickettsial population is well known. For example, actin-based motility is highly heterogeneous with motile bacteria present only 2% of the time at early stages versus 17% of the time at later stages of infection (Reed et al., 2014). Despite these low frequencies, loss of motility reduces virulence (Kleba et al., 2010), highlighting the importance of studying variable phenotypes in the rickettsial population.

We observed an inverse relationship between actin-based motility and BERC formation, as the tail-less mutant *sca2::Tn*

shows roughly 25-fold more interactions with the ER than WT *R. parkeri*. One of two scenarios could explain this observation: lacking actin-based motility increases the likelihood of a bacterium forming BERCs or decreases the chances of escaping BERCs once they are formed. Additionally, the bimodal phenotype of BERC formation observed with the *sca2::Tn* mutant indicates that motility is not the only layer of regulation. Understanding the role motility plays and what triggers BERC formation through host- or bacterial-specific mechanisms should elucidate whether BERC formation is driven by a subset of bacteria or if all bacteria can form BERCs but do so at different phases of their life cycle.

It is unlikely that BERCs grossly impair bacterial survival through processes such as autophagy because BERCs were not correlated with lower bacterial burdens and BERC frequency did not increase when the autophagosome-targeted *ompB::Tn* mutant (Engström et al., 2019) was tested. Moreover, decreasing BERC frequency via VAP depletion does not alter bacterial loads. In addition to autophagy, the ER regulates lipid metabolism, organelle trafficking, carbohydrate metabolism, apoptosis, inflammasome formation, and calcium signaling (Prinz et al., 2020; Wu et al., 2018). The obligate lifestyle of *R. parkeri* highlights that these

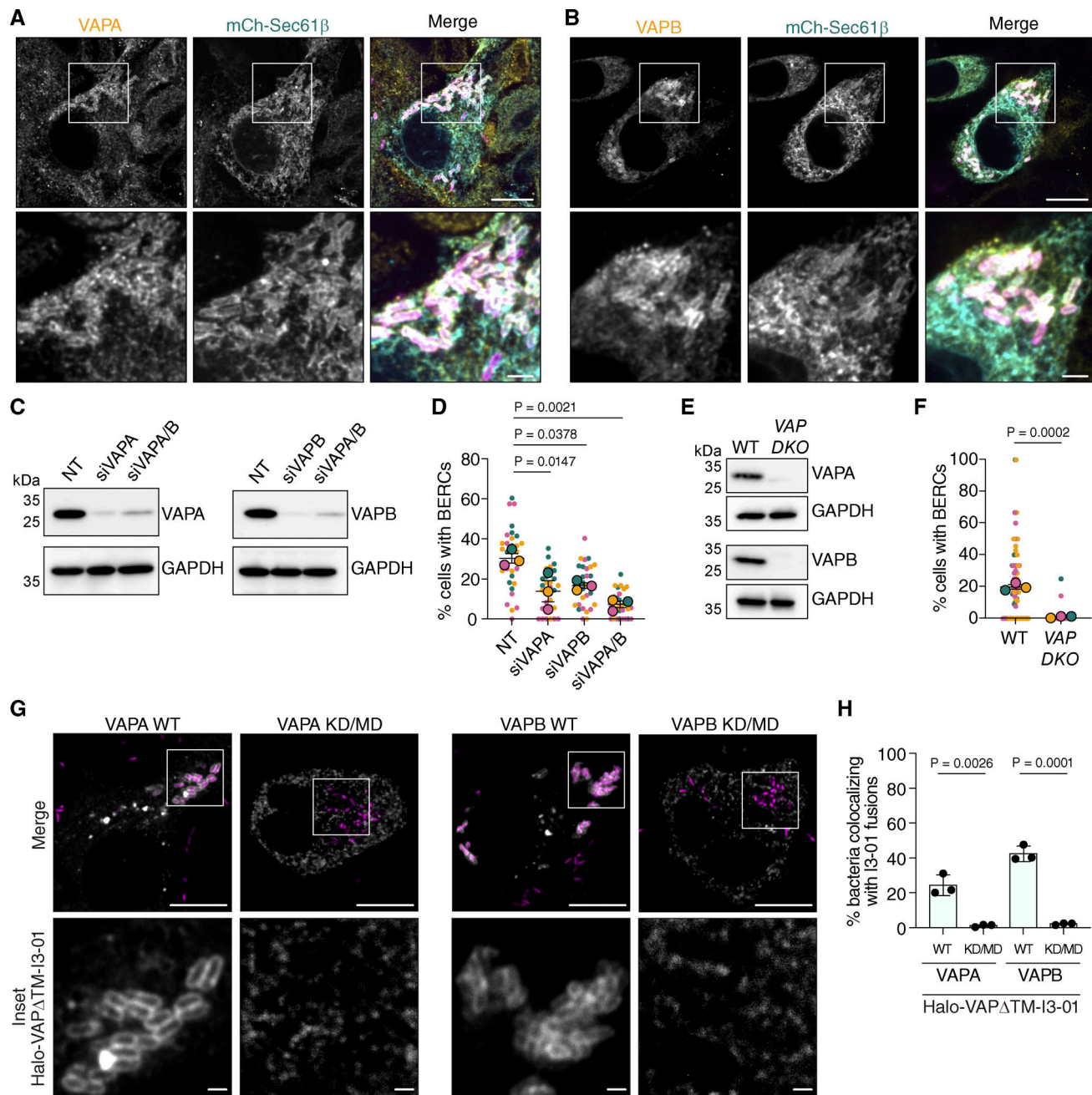


**Figure 5. Interactions between *R. parkeri* and the ER are dependent on VAPA and VAPB.** (A and B) Immunofluorescence detection of endogenous VAPA or VAPB localization around *sca2*::Tn mutant bacteria (magenta) at 24 hpi. Images are representative of three independent experiments. Scale bar, 10 μm; inset scale bar, 1 μm. (C) Western blot analysis of A549-mCh-Sec61β cell lysates after indicated siRNA treatment at 72 h after transfection. GAPDH, loading control. (D) Percentage of A549-mCh-Sec61β cells displaying BERCS with *sca2*::Tn mutant bacteria at 24 hpi after the indicated siRNA treatment in C. (E) Western blot analysis of VAPA and VAPB expression in HeLa cell lysates from F. GAPDH, loading control. (F) Percentage of WT or VAPA/B DKO HeLa cells displaying BERCS with *sca2*::Tn mutant bacteria (28 hpi). For D and F, the mean ± SEM of three independent experiments (large outlined circles) are superimposed over the raw data the percent of cells with BERCS per FOV (small unlined circles) (>100 cells quantified per condition per independent experiment) (one-way ANOVA with Dunnett's post hoc test). (G) Live-cell imaging snapshots at 24 hpi of Halo-VAPAΔTM-I3-01 or Halo-VAPBΔTM-I3-01 (grey) fusions (WT versus KD/MD FFAT-binding mutant) during infection with *sca2*::Tn mutant bacteria (magenta). Scale bar, 10 μm; inset scale bar, 1 μm. (H) Percentage of *sca2*::Tn mutant bacteria in transiently transfected A549 cells showing Halo-VAPΔTM-I3-01 localization. Data are mean ± SD of three independent experiments (≥4 FOV with ≥200 bacteria quantified per condition per independent experiment) (unpaired two-tailed t test). Source data are available for this figure: SourceData F5.

pathogens are reliant on their host to survive, and one or more of these functions could be regulated by BERCS under specific conditions or in certain cell types. For example, BERCS might promote metabolite exchange between the ER and the bacterium, and it will

be important to investigate this possibility once our understanding of rickettsial metabolism improves. It is also possible that BERCS represent a unique adaptation to modulate host or bacterial function that remains to be identified.

Our discovery of a stable, interkingdom interaction between the bacterial pathogen *R. parkeri* and the ER challenges our traditional view of their cytosolic infectious life cycle. Indeed, this unique adaptation by *R. parkeri*, which was not found for other cytosolic pathogens we tested, exemplifies the exceptional strategies this pathogen has evolved and underscores the importance of better understanding its biology. It also remains to be seen if *R. parkeri* interacts with other organelle membranes, potentiating large-scale changes to the cellular landscape in favor of pathogen or host fitness. In the end, this work highlights an unexpected mode of host-pathogen interaction whose study may also deepen our understanding of ER function.

## Materials and methods

### Cell lines

A549 (human lung epithelial, RRID:CVCL\_A549), Vero (monkey kidney epithelial, RRID:CVCL\_0059), and HEK293T (human embryonic kidney, RRID:CVCL\_0063) cells were obtained from the University of California, Berkeley Cell Culture Facility (Berkeley, CA, USA). HMEC-1 (human microvascular endothelial cell line-1, RRID:CVCL\_0307) was a gift from Dr. Matthew Welch at the University of California (Berkeley, CA, USA). VAPA/B DKO HeLa cells (Dong et al., 2016) were a gift from Dr. Pietro De Camilli. ATG knockout HeLa cells (ATG5<sup>-/-</sup>) (Nezich et al., 2015) were a gift from Dr. Richard Youle at the National Institute of Neurological Disorders and Stroke (Bethesda, MD, USA). A549 cells, HEK293T cells, and HeLa cells were maintained in Dulbecco's modified Eagle's medium (DMEM, 11965118; Gibco), supplemented with 10% fetal bovine serum (FBS). Vero cells were maintained in DMEM supplemented with 5% FBS. HMEC-1 cells were maintained in MCDB 131 liquid medium with no glutamine (10372019; Thermo Fisher Scientific), supplemented with 10% FBS, 1 µg/ml hydrocortisone (50-23-7; Sigma-Aldrich), 10 ng/ml epidermal growth factor (354001; Corning), and 2 mM L-glutamine (56-85-9; Sigma-Aldrich).

A549 cells expressing mCherry-Sec61β or the BiP signal sequence fused to mNeonGreen were generated using lentiviral transduction, as previously described (Lamason et al., 2016). Briefly, the mCherry-Sec61β fusion was subcloned from mCh-Sec61β (49155; Addgene) into the lentiviral plasmid FCW2IB-LifeAct-mWasabi (Lamason et al., 2016) by replacing the LifeAct-mWasabi fusion, upstream of the IRES. For the BiP-mNeonGreen-KDEL fusion, the BiP signal sequence (Friedman et al., 2011) and a KDEL sequence were fused to the N- and C- termini of mNeonGreen, respectively. The BiP-mNeonGreen-KDEL fusion was then subcloned upstream of the IRES of FCW2IB-LifeAct-mWasabi by replacing the LifeAct-mWasabi fusion. Viral particles were packaged by transfecting HEK293T cells plated the day before at  $2.5 \times 10^5$  cells/ml (2 ml/well, 6-well plate) using calcium phosphate with 400 ng pMDL-RRE, 400 ng pCMV-VSVg, 400 ng RSV-Rev, and 800 ng FCW2IB-mCherry-Sec61β (or FCW2IB-BiP-mNeonGreen-KDEL). Roughly, 24 h after transfection, the media was replaced with 1.2 ml of fresh media to concentrate the virus. 48 h after transfection, the concentrated supernatant was filtered through a 0.45-µm syringe filter and added to A549 cells at  $\sim 2 \times 10^5$  cells/ml. After 24 h of adding the

filtered supernatant, cells were overlaid with fresh media containing 12 µg/ml of blasticidin (3513-03-9; Sigma-Aldrich).

To achieve similar fluorescence levels, A549-mCherrySec61β cells were sorted based on mCherry fluorescence using the FACS Aria II Cell Sorter (BD Biosciences) at the Whitehead Institute for Biomedical Research Flow Cytometry Core Facility (Cambridge, MA, USA). All sorted and parental cell lines were confirmed to be mycoplasma-negative in a MycoAlert PLUS assay (LT07-710; Lonza) performed by the Koch Institute High-Throughput Sciences Facility (Cambridge, MA, USA).

To generate HeLa cell lines (WT, VAP DKO, and ATG5<sup>-/-</sup>) expressing mCherry-Sec61β, viral particles were packaged by transfecting HEK293T cells plated the day before at  $7.5 \times 10^5$  cells/ml (2 ml/well, 6-well plate) using TransIT-LT1 transfection reagent (2300; Mirus Bio) with 625 ng pMDL-RRE, 625 ng pCMV-VSVg, 625 ng RSV-Rev, and 1,250 ng FCW2IB-mCherry-Sec61β, and centrifuged at  $1,000 \times g$  for 30 min. 6 h after transfection, the media was replaced with 5 ml fresh DMEM with 10% FBS and 1% bovine serum albumin (BSA) and incubated for 36 h. Viral supernatant was filtered through a 0.45-µm syringe filter and concentrated to 1/10 the original volume in fresh DMEM + 10% FBS using Lenti-X concentrator (631321; Takara Bio) following manufacturer protocols. 0.1 ml of concentrated virus, diluted to a final volume of 2 ml in DMEM + 10% FBS + 8 µg/ml polybrene (TR-1003-G; EMD Millipore), was added to HeLa cells seeded at  $9 \times 10^4$  cells/ml (2 ml/well, 6-well plate), centrifuged at  $1,000 \times g$  for 30 min, and incubated for 5 h. After initial incubation, cells were washed with PBS and were recovered in 2 ml fresh DMEM with 10% FBS for 24 h before adding 3 µg/ml blasticidin to select for mCherry-Sec61β expressing cells.

### Bacteria plasmids and strains used in this study

RpBFP (Lamason et al., 2016, 2018), the *sca2::Tn* mutant (Reed et al., 2014), the *ompB<sup>STOP</sup>::Tn* mutant (Engström et al., 2019; Lamason et al., 2018) (a kind gift from Dr. Matthew Welch), and the *sca2::Tn* transformed with pRAM18dSGA-OmpApr-GFPuv (*sca2::Tn* pRAM GFP) (Lamason et al., 2016) were generated as previously described. RpBFP refers to *R. parkeri* expressing two TagBFP cassettes cloned into pRAM18dRA (Lamason et al., 2016, 2018). All rickettsial strains were propagated at 33°C in Vero cells with DMEM containing 2% FBS and isolated by mechanical disruption, as previously described (Lamason et al., 2016, 2018). Bacteria were aliquoted in brain heart infusion media (BHI, DF0037-17-8; Thermo Fisher Scientific) and stored at -80°C to decrease variability between replicates due to freeze-thaw cycles. Bacterial titers were determined as previously described via plaque assay (Lamason et al., 2016).

The DasherGFP-expressing strain (LmDasher, strain PL1938 10403S:DasherGFP) was a kind gift from Dr. Erin Benanti (Aduro Biotech). To generate LmDasher, DasherGFP was codon-optimized for *L. monocytogenes* expression, cloned downstream of the *actA* promoter, and integrated at the tRNA-Arg locus using pPL2. *L. monocytogenes* strains were grown in BHI. The GFP *L. monocytogenes* ActA deletion strain ( $\Delta actA$ ) was a gift from Dr. Michelle Reniere (University of Washington) and Dr. Dan Portnoy (University of California Berkeley) and was generated by integrating

pPL2-gfp (Lauer et al., 2002) into the DP-L3078 ( $\Delta actA$ ) strain (Skoble et al., 2000).

WT *S. flexneri* 2457T (Labrec et al., 1964) and the isogenic IcsA mutant *icsA:: $\Omega$*  (specR) (Steinhauer et al., 1999) were gifts from Dr. Marcia Goldberg (Massachusetts General Hospital, Boston, MA, USA). *S. flexneri* strains were grown on tryptic soy agar supplemented with 0.01% Congo Red (LC133507; LabChem) and supplemented with 100  $\mu\text{g}/\mu\text{l}$  spectinomycin (22189-32-8; Sigma-Aldrich) or 100  $\mu\text{g}/\mu\text{l}$  ampicillin (69-52-3; Sigma-Aldrich) as needed. WT *S. flexneri* and 2457T *icsA:: $\Omega$*  (specR) were transfected with the GFPmut3-expressing plasmid pFPV25.1 (Rathman et al., 2000; Valdivia and Falkow, 1996) (20668; Addgene) using electroporation, as previously described (Warren, 2011).

### Live microscopy of bacterial infections

All experiments were imaged with the Olympus IXplore Spin microscope system using an environmental chamber set to 5%  $\text{CO}_2$  and 37°C for *L. monocytogenes* and *S. flexneri* infections or 33°C for *R. parkeri* infections. This system was also equipped with four lasers, a Yokogawa CSU-W1 spinning disc unit, and ORCA-Flash4.0 sCMOS camera. Movies were acquired using a 100 $\times$  UPlanSApo objective (1.35 numerical aperture) and Z Drift Compensation. Movies were deconvolved using Olympus CellSens software. All data quantification was performed in ImageJ, where bacteria were manually counted on the last frame of each movie.

To determine if *L. monocytogenes* interacts with the ER, 2 ml of BHI cultures were inoculated with *L. monocytogenes* and grown for 16–18 h overnight at 30°C without shaking. A549-mCh-Sec61 $\beta$  cells at  $2.5 \times 10^5$  cells/cm<sup>2</sup> were grown in 20-mm Mattek dishes (P35G-1.5-20-C; MatTek Corporation). Bacteria from 0.5 ml of culture grown overnight were pelleted by centrifugation at 10,000  $\times g$  for 30 s at room temperature and resuspended in 500  $\mu\text{l}$  PBS (Phosphate-buffered saline). Resuspended bacteria (LmDasher or  $\Delta actA$ ) were used to infect cells by adding suspension directly to cells at an MOI of 1–2. Infections were carried out at 37°C for at least 4 h before imaging. Before imaging, the dishes were washed two times and overlaid with FluoroBrite DMEM (A1896702; Thermo Fisher Scientific) containing 10% FBS. Movies were acquired at 20-s intervals for at least 3 min. Infections with both strains were imaged and >30 cells representing >1,000 total bacteria were imaged per strain for each replicate ( $n = 3$ ).

To determine if *S. flexneri* forms interactions with the ER, *S. flexneri* was grown overnight in tryptic soy broth at 37°C with shaking. Overnight cultures were subcultured 1:200 and grown at 37°C with shaking for 2–3 h until cultures reached exponential phase ( $\text{OD}_{600} \approx 0.4$ – $0.6$ ). Bacteria from 1 ml of culture were pelleted by centrifugation and resuspended in 250  $\mu\text{l}$  PBS. Resuspended bacteria were used to infect A549-mCh-Sec61 $\beta$  cells at  $0.6 \times 10^5$  cells/cm<sup>2</sup> in an 8-well chambered coverglass with a No. 1.5 borosilicate glass bottom (155360; Thermo Fisher Scientific) at an MOI of 100. Infected cells were incubated for 30 min at 37°C and 5%  $\text{CO}_2$ . Cells were washed twice with warm PBS and media was replaced with FluoroBrite DMEM containing 10% FBS and 25  $\mu\text{g}/\text{ml}$  gentamicin. Cells were incubated for an

additional 1–1.5 h until intracellular bacteria were clearly visible. Movie acquisition and processing were done as with *L. monocytogenes* infections.

To determine the frequency of ER-rickettsia interactions, A549-mCh-Sec61 $\beta$  cells on 8-well chambered coverglass (at  $0.6 \times 10^5$  cells/cm<sup>2</sup>) were infected with RpBFP (WT), *sca2::Tn* (*sca2::Tn* pRAM-GFP), or *ompB::Tn* (*ompB<sup>STOP</sup>::Tn*) at an MOI of 0.5–2 for 28 and 48 h at 33°C (note, *R. parkeri* requires a longer incubation to accommodate its slower replication rate relative to *L. monocytogenes* and *S. flexneri*). Before imaging, each well was washed two times and overlaid with FluoroBrite DMEM containing 10% FBS. Movies were collected at 20-s intervals for at least 3 min. Approximately 10 fields of view (FOVs) were imaged for each replicate ( $n = 3$ ) and >2,000 bacteria were quantified. To determine the frequency of host cells displaying BERCS, three replicates were manually quantified on ImageJ representing a total of 30 FOVs and >50 cells.

To visualize actin dynamics in the context of ER-rickettsia interactions, A549-BiP-mNeonGreen-KDEL cells on 8-well chambered coverglass (at  $0.6 \times 10^5$  cells/cm<sup>2</sup>) were infected at an MOI of 0.5–1 with RpBFP and incubated at 33°C for 48 h. Before imaging, each well was washed two times with FluoroBrite DMEM containing 10% FBS. Then, cells were overlaid with SIR-Actin (CY-SC001; Cytoskeleton) at a final concentration of 1  $\mu\text{M}$  in FluoroBrite DMEM containing 10% FBS and incubated for 1 h. Imaging was done as described above for live-cell imaging of rickettsial infections. Approximately 10 FOVs were imaged per strain for each replicate ( $n = 2$ ) and >100 bacteria interacting with the ER were quantified.

To determine the stability of ER interactions with the WT or *sca2::Tn* mutant rickettsiae over a 1-h period, A549-mCh-Sec61 $\beta$  cells ( $2.5 \times 10^5$  cells/cm<sup>2</sup>) in an 8-well chambered coverglass were infected by centrifuging cells at 200  $\times g$  for 5 min at room temperature with an MOI of 1.5–2. Infected cells were incubated at 33°C for 24 h, and imaging proceeded as above for rickettsial infections. Approximately 10 infected cells displaying ER interactions with rickettsiae were imaged per replicate ( $n = 3$ ). Movies were captured at 5-min intervals and ER interactions were tracked over the 1 h period. >20 cells were quantified per replicate.

To determine the frequency of ER-rickettsia interactions after loss of ATG5, WT, and *ATG5<sup>-/-</sup>* HeLa-mCh-Sec61 $\beta$  cells ( $1.25 \times 10^5$  cells/cm<sup>2</sup>) in an 8-well chambered coverglass were infected by centrifuging cells at 300  $\times g$  for 5 min at room temperature with an MOI of 1–2. Infected cells were incubated at 33°C for 48 h, and imaging proceeded as above for rickettsial infections. At least 10 FOVs were imaged for each replicate ( $n = 3$ ), and the frequency of BERC-positive cells was manually quantified on ImageJ, representing >30 FOVs and >270 cells per condition.

### TEM

A549 and HMEC-1 cells seeded at  $\sim 3.0 \times 10^5$  or  $1.5 \times 10^5$  cells/cm<sup>2</sup>, respectively, in a 10-cm<sup>2</sup> dish were infected with the *sca2::Tn* mutant at an MOI of 0.5–1. Briefly, media was aspirated from cells, and cells were washed one time with PBS and overlaid with 1 ml of BHI covering the entire layer of cells. Then, the bacteria were added to cells and incubated via slow rocking at 37°C for

30 min. After, the infected cells were overlaid with DMEM containing 10% FBS (A549) or MCDB 131 liquid medium without glutamine, supplemented as described above (HMEC-1), and incubated at 33°C for 30 h. Cells were then fixed using Karnovsky Fixative Reagent Grade (3% glutaraldehyde and 2% formaldehyde in 0.1 M phosphate buffer, pH 7.4) (15732-10; Electron Microscopy Sciences) for 1 h at room temperature. After incubation, cells were scraped and centrifuged at  $10,000 \times g$  for 5 min at room temperature in 50-ml conicals. The pellet was transferred to a 1.5-ml Eppendorf, where it was centrifuged again at  $10,000 \times g$  for 2 min at room temperature and stored in fresh Karnovsky Fixative Reagent at 4°C until embedding.

Fixed cells were postfixed in 1% osmium tetroxide in veronal-acetate buffer. The cells were stained en block overnight with 0.5% uranyl acetate in veronal-acetate buffer (pH 6.0), and then dehydrated and embedded in Embed-812 resin. Sections were cut on a Leica Ultra Microtome with a diatom diamond knife at a thickness setting of 50 nm and stained with 2% uranyl acetate and lead citrate. The sections were examined using a Hitachi 7800 TEM 80KV and photographed with an AMT CCD camera. Sample preparation after fixation and imaging was performed at the Harvard University Center for Nanoscale Systems (Cambridge and Allston, MA, USA). Two replicates were performed per cell line.

2D morphometric analysis to determine the percent bacterial or mitochondrial perimeter covered by the ER as well as the average distance between the ER and bacterial or mitochondrial membrane was performed in A549 cells by tracing the subcellular structures in Image J. To determine the average distance between the ER and bacterial or mitochondrial membrane, distances were quantified every 100 nm for ER membranes that were separated  $\leq 130$  nm from the surface of either bacteria or mitochondria. To determine the percent perimeter covered, the bacterial and mitochondrial surface that was  $\leq 130$  nm from an ER membrane was traced. Approximately  $>10$  bacteria and  $>10$  mitochondria were quantified per replicate ( $n = 2$ ).

### FIB-SEM

To locate an infected cell for 3D FIB-SEM imaging, a thin plastic section was lifted off the block face using a microtome knife, transferred onto a TEM grid, and scanned in a TEM for the presence of bacteria (Leica Ultramicrotome, 7800 TEM; Hitachi). To reduce the search area and facilitate determining the orientation of the thin section, the block was trimmed prior to a trapezoidal cross-section with an approximate edge length of 500  $\mu\text{m}$ . Once a cell with the desired ultrastructure was identified, a series of images were recorded at cascading magnifications keeping the region of interest in the image center. The magnification was lowered until a block edge or corner was visible in the image. This approach made it possible to start the search in the SEM on an easily recognizable region of the block and use characteristic features at varying length scales in the corresponding back-scatter image to trace a path back to the actual region of interest.

FIB-SEM data were acquired on a Zeiss Crossbeam 550 using the Atlas software package. The cell was prepared for automatic serial sectioning by first covering its visible region with a 1- $\mu\text{m}$ -

thick Pt film via ion beam-assisted deposition. A series of line markings carved into the film with the ion beam act as fiducial markers for drift correction and the measurement of the progression of the ion beam during the run. The grooves are subsequently covered with a 1- $\mu\text{m}$ -thick carbon film to reduce curtaining artifacts, generate contrast, and ultimately preserve the markings throughout the run. After clearing material in front of the region of interest to a visual depth of 20  $\mu\text{m}$ , data were recorded using the energy-selective back-scatter detector with the electron beam operating at 1.5 kV and 2 nA. Cross-section images with a 5-nm pixel size and a dwell time of 10  $\mu\text{s}$  were recorded in 10 nm slice intervals. Milling was performed with the ion beam set to 30 kV and a current of 700 pA.

Images were aligned via cross-correlation and denoised with the non-local means filter using an in-house Matlab-based software package. Due to the relatively long dwell time, images contained small distortions along the slow scan direction. A stripe-based cross-correlation approach was designed to carefully measure displacements within stripes of consecutive images, which allowed to construct a displacement field for each image that was subsequently used to correct for locally varying drift and to ensure exact alignment throughout the volume of the dataset. Analysis scripts are available upon request through the corresponding author. The final data volume of  $15 \times 15 \times 15 \mu\text{m}^3$  ultimately contained 17 bacteria enveloped by the cell ER. Deep-learning data segmentation was performed using the Object Research Systems (ORS) Dragonfly software to extract the organelles of interest. A U-Net model with five depth levels, a starting number of 64 convolutional kernels, and a patch size of 64 pixels was successfully trained using three manually segmented image slices. The model was then applied to the rest of the FIB-SEM image stack. 3D models were generated using the segmentation data and the 3D visualizer in ORS Dragonfly.

### Endogenous p62 and VAP localization assays

A549-BiP-mNeonGreen-KDEL cells were seeded at  $4 \times 10^5$  cells/ml (0.5 ml/well, 24-well plate) on glass coverslips. The next day, cells were infected by centrifugation at  $200 \times g$  for 5 min at room temperature with an MOI of 1–2 (for strains: RpBFP, *sca2::Tn* mutant, or *ompB::Tn* mutant) and incubated at 33°C for 24 h. Following infection, infected cells were fixed in 4% paraformaldehyde (PFA) for 1 h by removing 0.2 ml of media and adding 0.3 ml of 8% PFA diluted in DMEM + 10% FBS. Fixed cells were incubated in 0.1 M glycine for 10 min at room temperature to quench residual PFA and then washed three times with PBS. For staining of endogenous p62, cells were permeabilized with 0.5% triton X-100 in PBS for 5 min and then washed three times in PBS. Samples were blocked for 1 h in a blocking buffer (2% BSA and 10% normal goat serum in PBS). Samples were then incubated for 1 h with mouse anti-p62 (610833; BD Transduction Laboratories) and rabbit anti-Rickettsia I7205 (kindly provided by Dr. Ted Hackstadt) diluted 1/200 and 1/500, respectively, in blocking buffer. Samples were then washed three times with PBS and incubated for 1 h in goat anti-mouse conjugated to Alexa Fluor 647 (A-21236; Invitrogen) and goat anti-rabbit conjugated to Alexa Fluor 405 (A-31556; Invitrogen), both diluted 1/200 in blocking buffer. Coverslips were then washed three times with

PBS and then mounted on glass slides using ProLong Gold Antifade Mountant (P36934; Invitrogen). For staining of endogenous VAPs, cells were permeabilized with 10  $\mu\text{g/ml}$  digitonin in PBS and incubated for 15 min, as previously demonstrated for imaging endogenous VAPs (Zhao et al., 2018). Samples were then blocked for 1 h in blocking buffer before being incubated overnight at 4°C in blocking buffer with either 1/200 diluted rabbit anti-VAPA (15275-1-AP; Proteintech) or 1/100 diluted rabbit anti-VAPB (144-77-1-AP; Proteintech) with 1/1,000 diluted mouse anti-Rickettsia 14-13. The next day coverslips were washed three times with PBS and then incubated for 1 h at room temperature with goat anti-mouse conjugated to Alexa Fluor 405 (A-31553; Invitrogen) and goat anti-rabbit conjugated to Alexa Fluor 647 (A-21244; Invitrogen), both diluted 1/200 in blocking buffer. Coverslips were then washed in PBS and mounted on glass slides as described above.

All fixed and stained coverslips were imaged with the Olympus IXplore Spin microscope system using a 100 $\times$  objective. Both p62 and VAP localization are expressed as a percent total of all counted *R. parkeri* within an independent experiment. All data were quantified manually using ImageJ with  $\geq 4$  FOV counted containing a total of  $\geq 200$  bacteria per independent experiment ( $n = 3$ ).

#### Exogenous VAP localization assays

A549-mCh-Sec61 $\beta$  cells were grown on an 8-well chambered coverglass (at  $1.2 \times 10^5$  cells/cm<sup>2</sup>) and were transfected the next day with 250 ng of HaloTag-VAPA or HaloTag-VAPB construct (a kind gift from Dr. Jennifer Lippincott-Schwartz) (Obara et al., 2024) using Lipofectamine 3000 (catalog number L3000001; Thermo Fisher Scientific) following the manufacturer's instructions. After 4 h, cells were washed twice with warm PBS and the media was replaced with fresh DMEM containing 10% FBS. At 8 h after transfection, cells were infected by centrifugation at  $200 \times g$  for 5 min at room temperature with an MOI of 2-3. Infected cells were incubated at 33°C for an additional 12 h. Before imaging, media was replaced with FluoroBrite DMEM containing 10% FBS and 50 nM of the fluorogenic dye JF635-HaloTag ligand (Janelia Materials), and cells were incubated at 33°C for 30 min, followed by two washes and overlay with FluoroBrite DMEM containing 10% FBS. Live-cell imaging proceeded as described above for rickettsial infections. Approximately 15 HaloTag expressing, infected cells displaying ER interactions with the *sca2::Tn* mutant were imaged per replicate ( $n = 3$ ).

To examine exogenous VAP localization frequency independent of their ER localization, HaloTag-VAPA and HaloTag-VAPB were first subcloned without their ER transmembrane domains (aka "VAP $\Delta$ TM"; amino acids 228-248 of VAPA and amino acids 223-243 of VAPB). The C-terminal domain of these mutants was then fused to the I3-01 oligomerization domain (Hsia et al., 2016). HaloTag-VAPA $\Delta$ TM and HaloTag-VAPB $\Delta$ TM KD/MD mutants were similarly generated by first fusing a HaloTag to VAPA or VAPB KD/MD mutants without their ER transmembrane domains using pEGFPC1-hVAP-A KD/MD (mutant K94D/M96D, unable to bind FFAT motifs) (#104449; Addgene) or pEGFPC1-hVAP-B KD/MD (mutant K87D/M89D, unable to bind FFAT motifs) (#104450; Addgene) as a template. A549-mCh-

Sec61 $\beta$  cells or A549 cells grown on an 8-well chambered coverglass (at  $1.2 \times 10^5$  cells/cm<sup>2</sup>) were first infected with *sca2::Tn* mutant bacteria as above at an MOI of 1-2. At 6 hpi, 750 ng of the I3-01 fusion constructs were transfected into cells. At 12 h after transfection, HaloTag labeling and live-cell imaging proceeded as described above. Data quantification was manually performed on ImageJ where the percent of bacteria colocalizing with I3-01 was quantified from at least four FOV representing  $\geq 200$  bacteria per replicate.

#### BERC quantification in VAPA- and VAPB-depleted cells

We first determined the frequency of cells containing BERCS using pooled siRNA-mediated silencing of VAPA or VAPB, similar to prior work (Derré et al., 2011). Here, A549-mCh-Sec61 $\beta$  at  $\sim 0.6 \times 10^5$  cells/cm<sup>2</sup> in an 8-well chambered coverglass were transfected with 10 nM of pooled siRNAs against VAPA (L-021382-00-0005; Horizon Discovery), VAPB (L-017795-00-0005; Horizon Discovery), or a non-target control (D-001810-10-05; Horizon Discovery) using Lipofectamine RNAiMAX Transfection Reagent (13778030; Thermo Fisher Scientific). Cells were grown for 48 h at 37°C. At 48 h after transfection, cells were infected at an MOI of 1.5-2 with the *sca2::Tn* mutant by centrifuging cells at  $200 \times g$  for 5 min at room temperature. The infected cells were then incubated at 33°C for 24 h. Imaging was performed as described above, with  $\sim 10$  FOV imaged per condition for each replicate ( $n = 3$ ) and  $>300$  cells quantified. Data quantification was manually performed on ImageJ where cells containing  $\geq 1$  BERC(s) were deemed BERC-positive and quantified per FOV.

To determine the frequency of cells containing BERCS in WT and VAPA/B DKO HeLa cells, cells were grown on an 8-well chambered coverglass (at  $1.2 \times 10^5$  cells/cm<sup>2</sup>) for 24 h. Then *sca2::Tn* mutant bacteria were used to infect cells by centrifugation at  $200 \times g$  for 5 min at room temperature with an MOI of 1-2. At 28 hpi, live-cell imaging proceeded as above for rickettsial infections. Approximately 15 FOVs imaged per condition for each replicate ( $n = 3$ ) and  $>700$  cells were quantified. Data quantification was manually performed on ImageJ where cells containing  $\geq 1$  BERC(s) were deemed BERC-positive and quantified per FOV.

VAPA (L-021382-00-0005; Horizon Discovery) target sequences:

5'-CCUGAGAGAUGAAGGUUUA-3'  
5'-UAGGGAAAUUCAUCUUGUA-3'  
5'-GGAUAAACCGGAUCAACC-3'  
5'-GGCAAACCGAUGAAUUA-3'

VAPB (L-017795-00-0005; Horizon Discovery) target sequences:

5'-UGUUACAGCCUUCGAUUA-3'  
5'-CCACGUAGGUACUGUGUGA-3'  
5'-GCUCUUGGCUCUGGUGUU-3'  
5'-GUAUUUAUUGGAAGAUUG-3'

#### Western blot

To confirm siRNA-mediated silencing of VAPA and VAPB expression, transfections were completed as above except cells were plated in 24-well dishes. Cells were collected at 48 and 72 h

and lysed on ice for 10 min in immunoprecipitation lysis buffer (50 mM HEPES, 150 mM NaCl, 1 mM EDTA, 10% glycerol, 1% IGEPAL). The cell debris was then cleared via centrifugation at  $16,100 \times g$  4°C for 10 min. Lysates were analyzed by western blotting using rabbit anti-VAPA (15275-1-AP; Proteintech) and mouse anti-VAPB (66191-1-Ig; Proteintech) and rabbit anti-GAPDH (2118S, RRID:AB\_561053; Cell Signaling). Acquisition of blot images was performed on a BioRad ChemiDoc MP Imaging System.

To confirm loss of *ATG5*, *VAPA*, and *VAPB* expression in the indicated knockout lines, lysates were collected as described above and analyzed by western blotting using rabbit anti-ATG5 (12994T, RRID:AB\_2630393; Cell Signaling Technology), rabbit anti-VAPA (15275-1-AP; Proteintech), mouse anti-VAPB (66191-1-Ig; Proteintech), and rabbit anti-GAPDH (2118S; Cell Signaling).

### Statistics

The statistical analysis and significance are noted in the figure legends for each respective graph. Data are determined to be statistically significant when  $P < 0.05$  by unpaired *t* test (two-tailed) and one-way ANOVA with post hoc Dunnett's test. Statistical analyses and tests for normality (via Shapiro-Wilk or Kolmogorov-Smirnov tests) were performed using GraphPad PRISM 9. For combined replicate experiments, data distribution was assumed to be normal but this could not be formally tested.

### Online supplemental material

**Fig. S1** shows vacuole-like rickettsia-ER interactions with the BiP-mNeonGreen-KDEL ER marker, and the absence of interactions between the ER and *L. monocytogenes* or *S. flexneri*. **Fig. S2** shows p62 localization across three rickettsial strains, the frequency of ER interactions in *ATG5*<sup>-/-</sup> cells, the expression of *ATG* via western blot, and the frequency of rickettsia-ER interactions by the *ompB::Tn* strain. **Fig. S3** shows the bacterial burdens per cell in RNAi-treated or VAP DKO cells, along with the localization of overexpressed full-length Halo-VAP fusions. **Videos 1, 2, and 3** show live-cell imaging of rickettsia-ER interactions. **Videos 4 and 5** show segmented FIB-SEM image stacks of rickettsia-ER interactions.

### Data availability

The data generated and analyzed in this study are available from the corresponding author upon request. Further information and requests for reagents may be directed to and will be fulfilled by R.L. Lamason, [rlamason@mit.edu](mailto:rlamason@mit.edu).

### Acknowledgments

We thank Matt Welch (UC Berkeley, Berkeley, CA, USA), Erin Benanti (UC Berkeley, Berkeley, CA, USA), Michelle Reniere (University of Washington, Seattle, WA, USA), Dan Portnoy (UC Berkeley, Berkeley, CA, USA), Jennifer Lippincott-Schwartz (HHMI Janelia Research Campus, Ashburn, VA, USA), Marcia Goldberg (Harvard Medical School, Boston, MA, USA), Iain Cheeseman (Whitehead Institute, Cambridge, MA, USA), and Pietro De Camilli (Yale School of Medicine, New Haven, CT, USA) for the reagents.

We thank Jon McGinn, Iain Cheeseman, Adam Martin, and Allison Scott for critical feedback on the manuscript. We thank Nicki Watson for help preparing and imaging the TEM samples.

This work was performed in part at the Harvard University Center for Nanoscale Systems, a member of the National Nanotechnology Coordinated Infrastructure Network, which is supported by the National Science Foundation award no. ECCS-2025158. This work was also performed in part at the Flow Cytometry Core Facility at the Whitehead Institute for Biomedical Research. This work was supported in part by National Institutes of Health Grants no. T32GM007287 (Y. Acevedo-Sánchez), R01GM141025 (R.L. Lamason), and R01AI155489 (R.L. Lamason).

**Author contributions:** Y. Acevedo-Sánchez: Conceptualization, Data curation, Formal analysis, Funding acquisition, Investigation, Methodology, Project administration, Resources, Software, Supervision, Validation, Visualization, Writing - original draft, Writing - review & editing, P.J. Woida: Conceptualization, Data curation, Formal analysis, Investigation, Methodology, Visualization, Writing - original draft, Writing - review & editing, C. Anderson: Data curation, Formal analysis, Investigation, Methodology, Validation, Visualization, Writing - review & editing, S. Kraemer: Data curation, Formal analysis, Methodology, Resources, Software, Writing - review & editing, R.L. Lamason: Conceptualization, Data curation, Formal analysis, Funding acquisition, Investigation, Methodology, Project administration, Resources, Supervision, Validation, Visualization, Writing - original draft, Writing - review & editing.

**Disclosures:** The authors declare no competing interests exist.

Submitted: 21 June 2024

Revised: 25 November 2024

Accepted: 10 December 2024

### References

- Alpy, F., A. Rousseau, Y. Schwab, F. Legueux, I. Stoll, C. Wendling, C. Spiegelhalter, P. Kessler, C. Mathelin, M.-C. Rio, et al. 2013. STARD3/STARD3NL and VAP make a novel molecular tether between late endosomes and the ER. *J. Cell Sci.* 126:5500–5512. <https://doi.org/10.1242/jcs.139295>
- Anastasia, I., N. Ilacqua, A. Raimondi, P. Lemieux, R. Ghandehari-Alavijeh, G. Faure, S.L. Mekhedov, K.J. Williams, F. Caicci, G. Valle, et al. 2021. Mitochondria-rough-ER contacts in the liver regulate systemic lipid homeostasis. *Cell Rep.* 34:108873. <https://doi.org/10.1016/j.celrep.2021.108873>
- Barman, B., B.H. Sung, E. Krystofiak, J. Ping, M. Ramirez, B. Millis, R. Allen, N. Prasad, S. Chetyrkin, M.W. Calcutt, et al. 2022. VAP-A and its binding partner CERT drive biogenesis of RNA-containing extracellular vesicles at ER membrane contact sites. *Dev. Cell.* 57:974–994.e8. <https://doi.org/10.1016/j.devcel.2022.03.012>
- Bernardini, M.L., J. Mounier, H. d'Hauteville, M. Coquis-Rondon, and P.J. Sansonetti. 1989. Identification of icsA, a plasmid locus of *Shigella flexneri* that governs bacterial intra- and intercellular spread through interaction with F-actin. *Proc. Natl. Acad. Sci. USA.* 86:3867–3871. <https://doi.org/10.1073/pnas.86.10.3867>
- Bradford, W.D., B.P. Croker, and C.C. Tisher. 1979. Kidney lesions in rocky mountain spotted fever: A light-, immunofluorescence-, and electron-microscopic study. *Am. J. Pathol.* 97:381–392.
- Cardoen, B., K.R. Vandevorde, G. Gao, M. Ortiz-Silva, P. Alan, W. Liu, E. Tiliakou, A.W. Vogl, G. Hamarneh, and I.R. Nabi. 2024. Membrane

- contact site detection (MCS-DETECT) reveals dual control of rough mitochondria-ER contacts. *J. Cell Biol.* 223:e202206109. <https://doi.org/10.1083/jcb.202206109>
- Cook, K.C., E. Tsopurashvili, J.M. Needham, S.R. Thompson, and I.M. Cristea. 2022. Restructured membrane contacts rewire organelles for human cytomegalovirus infection. *Nat. Commun.* 13:4720. <https://doi.org/10.1038/s41467-022-32488-6>
- Costello, J.L., I.G. Castro, C. Hacker, T.A. Schrader, J. Metz, D. Zeuschner, A.S. Azadi, L.F. Godinho, V. Costina, P. Findeisen, et al. 2017. ACBD5 and VAPB mediate membrane associations between peroxisomes and the ER. *J. Cell Biol.* 216:331-342. <https://doi.org/10.1083/jcb.201607055>
- Dai, J., K.-H. Kuo, J.M. Leo, C. van Breemen, and C.-H. Lee. 2005. Rearrangement of the close contact between the mitochondria and the sarcoplasmic reticulum in airway smooth muscle. *Cell Calcium.* 37:333-340. <https://doi.org/10.1016/j.ceca.2004.12.002>
- De Vos, K.J., G.M. Mórotz, R. Stoica, E.L. Tudor, K.-F. Lau, S. Ackerley, A. Warley, C.E. Shaw, and C.C.J. Miller. 2012. VAPB interacts with the mitochondrial protein PTPIP51 to regulate calcium homeostasis. *Hum. Mol. Genet.* 21:1299-1311. <https://doi.org/10.1093/hmg/ddr559>
- Derré, I., R. Swiss, and H. Agaisse. 2011. The lipid transfer protein CERT interacts with the Chlamydia inclusion protein IncD and participates to ER-Chlamydia inclusion membrane contact sites. *PLoS Pathog.* 7:e1002092. <https://doi.org/10.1371/journal.ppat.1002092>
- Di Mattia, T., A. Martinet, S. Ikhlef, A.G. McEwen, Y. Nominé, C. Wendling, P. Poussin-Courmontagne, L. Voilquin, P. Eberling, F. Ruffenach, et al. 2020. FFAT motif phosphorylation controls formation and lipid transfer function of inter-organelle contacts. *EMBO J.* 39:e104369. <https://doi.org/10.15252/emj.2019104369>
- Domann, E., J. Wehland, M. Rohde, S. Pistor, M. Hartl, W. Goebel, M. Leimeister-Wächter, M. Wuenscher, and T. Chakraborty. 1992. A novel bacterial virulence gene in *Listeria monocytogenes* required for host cell microfilament interaction with homology to the proline-rich region of vinculin. *EMBO J.* 11:1981-1990. <https://doi.org/10.1002/j.1460-2075.1992.tb05252.x>
- Dong, R., Y. Saheki, S. Swarup, L. Lucast, J.W. Harper, and P. De Camilli. 2016. Endosome-ER contacts control actin nucleation and retromer function through VAP-dependent regulation of PI4P. *Cell.* 166:408-423. <https://doi.org/10.1016/j.cell.2016.06.037>
- Engström, P., T.P. Burke, G. Mitchell, N. Ingabire, K.G. Mark, G. Golovkine, A.T. Iavarone, M. Rape, J.S. Cox, and M.D. Welch. 2019. Evasion of autophagy mediated by *Rickettsia* surface protein OmpB is critical for virulence. *Nat. Microbiol.* 4:2538-2551. <https://doi.org/10.1038/s41564-019-0583-6>
- Friedman, J.R., L.L. Lackner, M. West, J.R. DiBenedetto, J. Nunnari, and G.K. Voeltz. 2011. ER tubules mark sites of mitochondrial division. *Science.* 334:358-362. <https://doi.org/10.1126/science.1207385>
- Giacomello, M., and L. Pellegrini. 2016. The coming of age of the mitochondria-ER contact: A matter of thickness. *Cell Death Differ.* 23:1417-1427. <https://doi.org/10.1038/cdd.2016.52>
- Guo, Y., D. Li, S. Zhang, Y. Yang, J.-J. Liu, X. Wang, C. Liu, D.E. Milkie, R.P. Moore, U.S. Tulu, et al. 2018. Visualizing intracellular organelle and cytoskeletal interactions at Nanoscale resolution on millisecond time-scales. *Cell.* 175:1430-1442.e17. <https://doi.org/10.1016/j.cell.2018.09.057>
- Haglund, C.M., J.E. Choe, C.T. Skau, D.R. Kovar, and M.D. Welch. 2010. *Rickettsia* Sca2 is a bacterial formin-like mediator of actin-based motility. *Nat. Cell Biol.* 12:1057-1063. <https://doi.org/10.1038/ncb2109>
- Hsia, Y., J.B. Bale, S. Gonen, D. Shi, W. Sheffler, K.K. Fong, U. Nattermann, C. Xu, P.-S. Huang, R. Ravichandran, et al. 2016. Corrigendum: Design of a hyperstable 60-subunit protein icosahedron. *Nature.* 540:150. <https://doi.org/10.1038/nature20108>
- Hung, V., S.S. Lam, N.D. Udeshi, T. Svinkina, G. Guzman, V.K. Mootha, S.A. Carr, and A.Y. Ting. 2017. Proteomic mapping of cytosol-facing outer mitochondrial and ER membranes in living human cells by proximity biotinylation. *Elife.* 6:e24463. <https://doi.org/10.7554/eLife.24463>
- Kaiser, S.E., J.H. Brickner, A.R. Reilein, T.D. Fenn, P. Walter, and A.T. Brunger. 2005. Structural basis of FFAT motif-mediated ER targeting. *Structure.* 13:1035-1045. <https://doi.org/10.1016/j.str.2005.04.010>
- Kim, J., K.J. Smith, R. Naefie, and H. Skelton. 2004. Histopathologic features of and lymphoid populations in the skin of patients with the spotted fever group of rickettsiae: Southern africa. *Int. J. Dermatol.* 43:188-194. <https://doi.org/10.1111/j.1365-4632.2004.01560.x>
- Kim, S., S.S. Leal, D. Ben Halevy, C.M. Gomes, and S. Lev. 2010. Structural requirements for VAP-B oligomerization and their implication in amyotrophic lateral sclerosis-associated VAP-B(P56S) neurotoxicity. *J. Biol. Chem.* 285:13839-13849. <https://doi.org/10.1074/jbc.M109.097345>
- Kleba, B., T.R. Clark, E.I. Lutter, D.W. Ellison, and T. Hackstadt. 2010. Disruption of the *Rickettsia rickettsii* Sca2 autotransporter inhibits actin-based motility. *Infect. Immun.* 78:2240-2247. <https://doi.org/10.1128/IAI.010010-10>
- Kocks, C., E. Gouin, M. Tabouret, P. Berche, H. Ohayon, and P. Cossart. 1992. *L. monocytogenes*-induced actin assembly requires the actA gene product, a surface protein. *Cell.* 68:521-531. [https://doi.org/10.1016/0092-8674\(92\)90188-1](https://doi.org/10.1016/0092-8674(92)90188-1)
- Kors, S., J.L. Costello, and M. Schrader. 2022. VAP proteins - from organelle tethers to pathogenic host interactors and their role in neuronal disease. *Front. Cell Dev. Biol.* 10:895856. <https://doi.org/10.3389/fcell.2022.895856>
- Labrec, E.H., H. Schneider, T.J. Magnani, and S.B. Formal. 1964. Epithelial cell penetration as an essential step in the pathogenesis of bacillary dysentery. *J. Bacteriol.* 88:1503-1518. <https://doi.org/10.1128/jb.88.5.1503-1518.1964>
- Lamason, R.L., and M.D. Welch. 2017. Actin-based motility and cell-to-cell spread of bacterial pathogens. *Curr. Opin. Microbiol.* 35:48-57. <https://doi.org/10.1016/j.mib.2016.11.007>
- Lamason, R.L., E. Bastounis, N.M. Kafai, R. Serrano, J.C. Del Álamo, J.A. Theriot, and M.D. Welch. 2016. *Rickettsia* Sca4 reduces vinculin-mediated intercellular tension to promote spread. *Cell.* 167:670-683.e10. <https://doi.org/10.1016/j.cell.2016.09.023>
- Lamason, R.L., N.M. Kafai, and M.D. Welch. 2018. A streamlined method for transposon mutagenesis of *Rickettsia parkeri* yields numerous mutations that impact infection. *PLoS One.* 13:e0197012. <https://doi.org/10.1371/journal.pone.0197012>
- Lauer, P., M.Y.N. Chow, M.J. Loessner, D.A. Portnoy, and R. Calendar. 2002. Construction, characterization, and use of two *Listeria monocytogenes* site-specific phage integration vectors. *J. Bacteriol.* 184:4177-4186. <https://doi.org/10.1128/JB.184.15.4177-4186.2002>
- Lee, J.E., P.I. Cathey, H. Wu, R. Parker, and G.K. Voeltz. 2020. Endoplasmic reticulum contact sites regulate the dynamics of membraneless organelles. *Science.* 367:eaay7108. <https://doi.org/10.1126/science.aay7108>
- Lehto, M., R. Hynynen, K. Karjalainen, E. Kuismanen, K. Hyvärinen, and V.M. Olkkonen. 2005. Targeting of OSBP-related protein 3 (ORP3) to endoplasmic reticulum and plasma membrane is controlled by multiple determinants. *Exp. Cell Res.* 310:445-462. <https://doi.org/10.1016/j.yexcr.2005.08.003>
- Loewen, C.J.R., A. Roy, and T.P. Levine. 2003. A conserved ER targeting motif in three families of lipid binding proteins and in Opilp binds VAP. *EMBO J.* 22:2025-2035. <https://doi.org/10.1093/emboj/cdg201>
- Lukinavičius, G., L. Reymond, E. D'Este, A. Masharina, F. Göttfert, H. Ta, A. Günther, M. Fournier, S. Rizzo, H. Waldmann, et al. 2014. Fluorogenic probes for live-cell imaging of the cytoskeleton. *Nat. Methods.* 11:731-733. <https://doi.org/10.1038/nmeth.2972>
- Makino, S., C. Sasakawa, K. Kamata, T. Kurata, and M. Yoshikawa. 1986. A genetic determinant required for continuous reinfection of adjacent cells on large plasmid in *S. flexneri* 2a. *Cell.* 46:551-555. [https://doi.org/10.1016/0092-8674\(86\)90880-9](https://doi.org/10.1016/0092-8674(86)90880-9)
- McGinn, J., and R.L. Lamason. 2021. The enigmatic biology of rickettsiae: Recent advances, open questions and outlook. *Pathog. Dis.* 79:ftab019. <https://doi.org/10.1093/femspd/ftab019>
- Munderloh, U.G., S.F. Hayes, J. Cummings, and T.J. Kurtti. 1998. Microscopy of spotted fever *Rickettsia* movement through tick cells. *Microsc. Microanal.* 4:115-121. <https://doi.org/10.1017/S1431927698980096>
- Nezich, C.L., C. Wang, A.I. Fogel, and R.J. Youle. 2015. MiT/TFE transcription factors are activated during mitophagy downstream of Parkin and Atg5. *J. Cell Biol.* 210:435-450. <https://doi.org/10.1083/jcb.201501002>
- Nishimura, Y., M. Hayashi, H. Inada, and T. Tanaka. 1999. Molecular cloning and characterization of mammalian homologues of vesicle-associated membrane protein-associated (VAMP-associated) proteins. *Biochem. Biophys. Res. Commun.* 254:21-26. <https://doi.org/10.1006/bbrc.1998.9876>
- Obara, C.J., J. Nixon-Abell, A.S. Moore, F. Riccio, D.P. Hoffman, G. Shtengel, C.S. Xu, K. Schaefer, H.A. Pasolli, J.-B. Masson, et al. 2024. Motion of VAPB molecules reveals ER-mitochondria contact site subdomains. *Nature.* 626:169-176. <https://doi.org/10.1038/s41586-023-06956-y>
- Parlakgöl, G., S. Pang, L.L. Artico, N. Min, E. Cagampang, R. Villa, R.L.S. Goncalves, G.Y. Lee, C.S. Xu, G.S. Hotamışlıgil, and A.P. Arruda. 2024. Spatial mapping of hepatic ER and mitochondria architecture reveals zonated remodeling in fasting and obesity. *Nat. Commun.* 15:3982. <https://doi.org/10.1038/s41467-024-48272-7>
- Paul, P., and B. Tiwari. 2023. Organelles are miscommunicating: Membrane contact sites getting hijacked by pathogens. *Virulence.* 14:2265095. <https://doi.org/10.1080/21505594.2023.2265095>

- Phillips, M.J., and G.K. Voeltz. 2016. Structure and function of ER membrane contact sites with other organelles. *Nat. Rev. Mol. Cell Biol.* 17:69–82. <https://doi.org/10.1038/nrm.2015.8>
- Prinz, W.A., A. Toulmay, and T. Balla. 2020. The functional universe of membrane contact sites. *Nat. Rev. Mol. Cell Biol.* 21:7–24. <https://doi.org/10.1038/s41580-019-0180-9>
- Raab, J.E., D.J. Hamilton, T.B. Harju, T.N. Huynh, and B.C. Russo. 2024. Pushing boundaries: Mechanisms enabling bacterial pathogens to spread between cells. *Infect. Immun.* 92:e0052423. <https://doi.org/10.1128/iai.00524-23>
- Rathman, M., N. Jourhi, A. Allaoui, P. Sansonetti, C. Parsot, and G. Tran Van Nhieu. 2000. The development of a FACS-based strategy for the isolation of *Shigella flexneri* mutants that are deficient in intercellular spread. *Mol. Microbiol.* 35:974–990. <https://doi.org/10.1046/j.1365-2958.2000.01770.x>
- Reed, S.C.O., R.L. Lamason, V.I. Risca, E. Abernathy, and M.D. Welch. 2014. Rickettsia actin-based motility occurs in distinct phases mediated by different actin nucleators. *Curr. Biol.* 24:98–103. <https://doi.org/10.1016/j.cub.2013.11.025>
- Rizzuto, R., P. Pinton, W. Carrington, F.S. Fay, K.E. Fogarty, L.M. Lifshitz, R.A. Tuft, and T. Pozzan. 1998. Close contacts with the endoplasmic reticulum as determinants of mitochondrial Ca<sup>2+</sup> responses. *Science*. 280:1763–1766. <https://doi.org/10.1126/science.280.5370.1763>
- Rocha, N., C. Kuijl, R. van der Kant, L. Janssen, D. Houben, H. Janssen, W. Zwart, and J. Neefjes. 2009. Cholesterol sensor ORPIL contacts the ER protein VAP to control Rab7-RILP-p150 Glued and late endosome positioning. *J. Cell Biol.* 185:1209–1225. <https://doi.org/10.1083/jcb.200811005>
- Roggli, V.L., S. Keener, W.D. Bradford, P.C. Pratt, and D.H. Walker. 1985. Pulmonary pathology of Rocky Mountain spotted fever (RMSF) in children. *Pediatr. Pathol.* 4:47–57. <https://doi.org/10.3109/15513818509025902>
- Rowland, A.A., P.J. Chitwood, M.J. Phillips, and G.K. Voeltz. 2014. ER contact sites define the position and timing of endosome fission. *Cell*. 159:1027–1041. <https://doi.org/10.1016/j.cell.2014.10.023>
- Scorrano, L., M.A. De Matteis, S. Emr, F. Giordano, G. Hajnóczky, B. Kornmann, L.L. Lackner, T.P. Levine, L. Pellegrini, K. Reinisch, et al. 2019. Coming together to define membrane contact sites. *Nat. Commun.* 10:1287. <https://doi.org/10.1038/s41467-019-09253-3>
- Silverman, D.J., and C.L. Wisseman Jr. 1979. In vitro studies of rickettsia-host cell interactions: Ultrastructural changes induced by Rickettsia rickettsii infection of chicken embryo fibroblasts. *Infect. Immun.* 26:714–727. <https://doi.org/10.1128/iai.26.2.714-727.1979>
- Sit, B., and R.L. Lamason. 2024. Pathogenic Rickettsia spp. as emerging models for bacterial biology. *J. Bacteriol.* 206:e0040423. <https://doi.org/10.1128/jb.00404-23>
- Skoble, J., D.A. Portnoy, and M.D. Welch. 2000. Three regions within ActA promote Arp2/3 complex-mediated actin nucleation and Listeria monocytogenes motility. *J. Cell Biol.* 150:527–538. <https://doi.org/10.1083/jcb.150.3.527>
- Stanhope, R., E. Flora, C. Bayne, and I. Derré. 2017. IncV, a FFAT motif-containing Chlamydia protein, tethers the endoplasmic reticulum to the pathogen-containing vacuole. *Proc. Natl. Acad. Sci. USA.* 114:12039–12044. <https://doi.org/10.1073/pnas.1709060114>
- Steinhauer, J., R. Agha, T. Pham, A.W. Varga, and M.B. Goldberg. 1999. The unipolar Shigella surface protein IcsA is targeted directly to the bacterial old pole: IcsP cleavage of IcsA occurs over the entire bacterial surface. *Mol. Microbiol.* 32:367–377. <https://doi.org/10.1046/j.1365-2958.1999.01356.x>
- Valdivia, R.H., and S. Falkow. 1996. Bacterial genetics by flow cytometry: Rapid isolation of Salmonella typhimurium acid-inducible promoters by differential fluorescence induction. *Mol. Microbiol.* 22:367–378. <https://doi.org/10.1046/j.1365-2958.1996.00120.x>
- Valm, A.M., S. Cohen, W.R. Legant, J. Melunis, U. Hershberg, E. Wait, A.R. Cohen, M.W. Davidson, E. Betzig, and J. Lippincott-Schwartz. 2017. Applying systems-level spectral imaging and analysis to reveal the organelle interactome. *Nature*. 546:162–167. <https://doi.org/10.1038/nature22369>
- Vance, J.E. 1990. Phospholipid synthesis in a membrane fraction associated with mitochondria. *J. Biol. Chem.* 265:7248–7256. [https://doi.org/10.1016/S0021-9258\(19\)39106-9](https://doi.org/10.1016/S0021-9258(19)39106-9)
- Voeltz, G.K., E.M. Sawyer, G. Hajnóczky, and W.A. Prinz. 2024. Making the connection: How membrane contact sites have changed our view of organelle biology. *Cell*. 187:257–270. <https://doi.org/10.1016/j.cell.2023.11.040>
- Vormittag, S., R.J. Ende, I. Derré, and H. Hilbi. 2023. Pathogen vacuole membrane contact sites - close encounters of the fifth kind. *MicroLife*. 4:uqad018. <https://doi.org/10.1093/femsml/uqad018>
- Walker, D.H., and N. Ismail. 2008. Emerging and re-emerging rickettsioses: Endothelial cell infection and early disease events. *Nat. Rev. Microbiol.* 6:375–386. <https://doi.org/10.1038/nrmicro1866>
- Walker, D.H., V.L. Popov, P.A. Crocquet-Valdes, C.J. Welsh, and H.M. Feng. 1997. Cytokine-induced, nitric oxide-dependent, intracellular antirickettsial activity of mouse endothelial cells. *Lab. Invest.* 76:129–138.
- Wang, P.T.C., P.O. Garcin, M. Fu, M. Masoudi, P. St-Pierre, N. Panté, and I.R. Nabi. 2015. Distinct mechanisms controlling rough and smooth endoplasmic reticulum contacts with mitochondria. *J. Cell Sci.* 128:2759–2765. <https://doi.org/10.1242/jcs.171132>
- Warren, D.J. 2011. Preparation of highly efficient electrocompetent Escherichia coli using glycerol/mannitol density step centrifugation. *Anal. Biochem.* 413:206–207. <https://doi.org/10.1016/j.ab.2011.02.036>
- Wu, H., P. Carvalho, and G.K. Voeltz. 2018. Here, there, and everywhere: The importance of ER membrane contact sites. *Science*. 361:eaan5835. <https://doi.org/10.1126/science.aan5835>
- Wyles, J.P., C.R. McMaster, and N.D. Ridgway. 2002. Vesicle-associated membrane protein-associated protein-A (VAP-A) interacts with the oxysterol-binding protein to modify export from the endoplasmic reticulum. *J. Biol. Chem.* 277:29908–29918. <https://doi.org/10.1074/jbc.M201191200>
- Zhao, Y.G., N. Liu, G. Miao, Y. Chen, H. Zhao, and H. Zhang. 2018. The ER contact proteins VAPA/B interact with multiple autophagy proteins to modulate autophagosome biogenesis. *Curr. Biol.* 28:1234–1245.e4. <https://doi.org/10.1016/j.cub.2018.03.002>
- Zurek, N., L. Sparks, and G. Voeltz. 2011. Reticulon short hairpin transmembrane domains are used to shape ER tubules. *Traffic*. 12:28–41. <https://doi.org/10.1111/j.1600-0854.2010.01134.x>

## Supplemental material

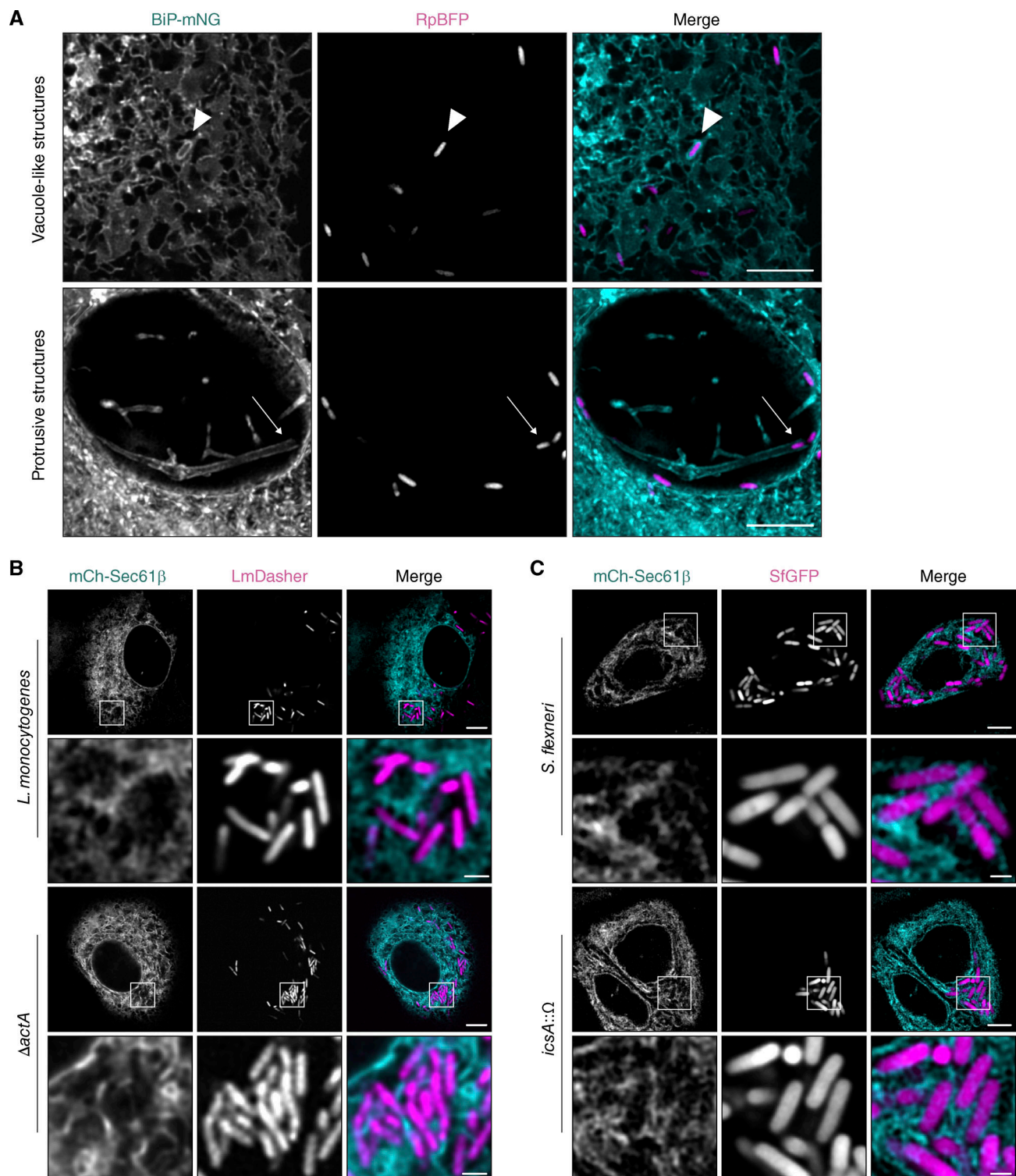


Figure S1. **Vacuole-like ER interactions are a unique adaptation by *R. parkeri*.** (A) Live-cell imaging snapshots of A549 cells expressing an ER marker (BiP-mNeonGreen-KDEL, cyan) infected with *R. parkeri* expressing BFP (magenta) at 28 hpi. The arrowhead in the inset points to *R. parkeri* in vacuole-like ER structure. Arrows in the inset point to *R. parkeri* in protrusive structures. Scale bars, 5  $\mu$ m. (B) Live-cell imaging snapshots at 4 hpi of A549-mCh-Sec61 $\beta$  cells (cyan) infected with DasherGFP-expressing WT or GFP-expressing  $\Delta actA$  mutant strains of *L. monocytogenes* (magenta). Scale bar, 5  $\mu$ m; inset, 1  $\mu$ m. (C) Live-cell imaging snapshots at 2 hpi of A549-mCh-Sec61 $\beta$  cells (cyan) infected with GFP-expressing WT or *icsA:: $\Omega$*  mutant strains of *S. flexneri* (magenta). Scale bar, 5  $\mu$ m; inset, 1  $\mu$ m. Data are representative of three independent experiments.

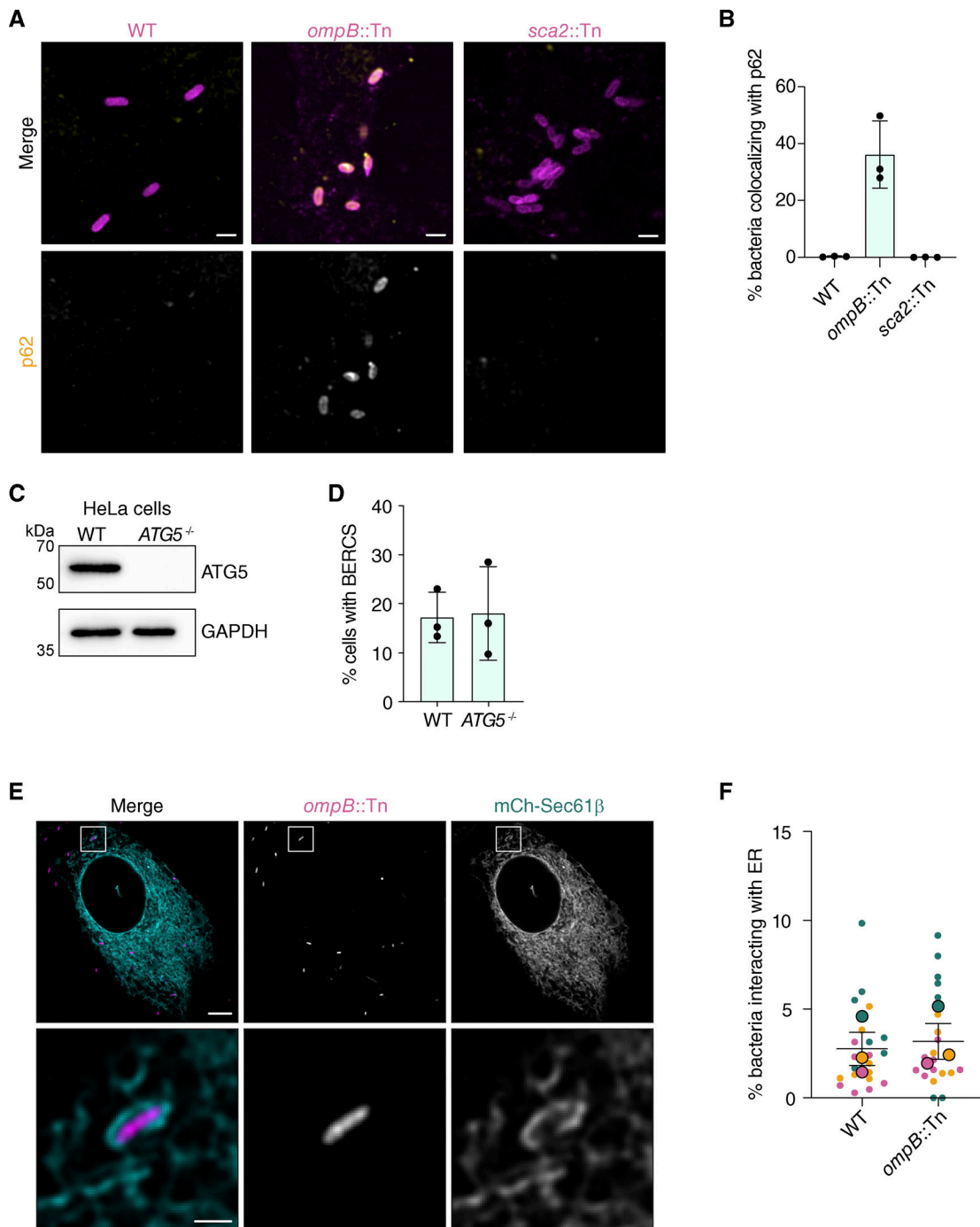
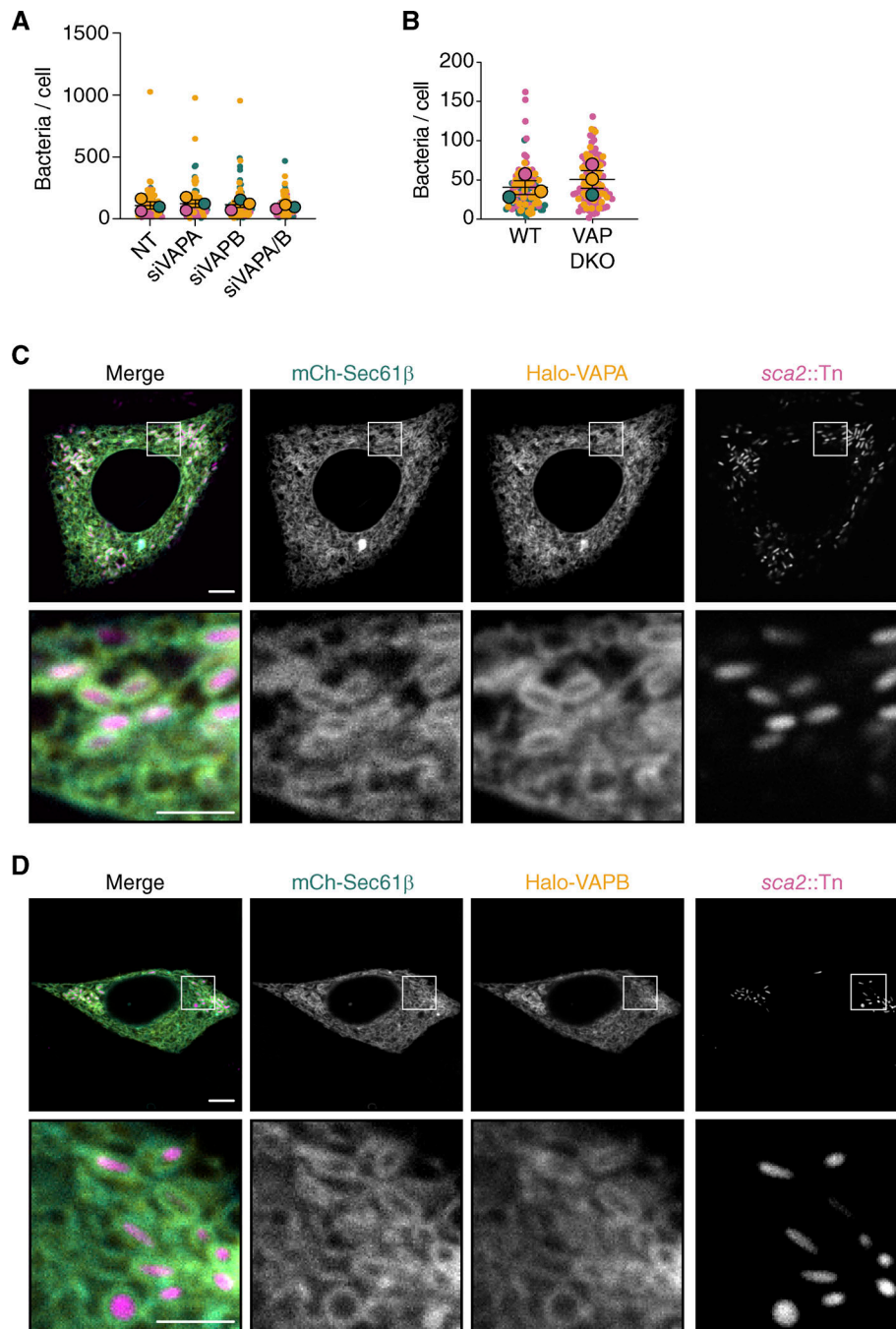


Figure S2. **The vacuole-like structures are not associated with the autophagic clearance of *R. parkeri*.** (A) Immunofluorescence microscopy of infected A549 cells at 24 hpi showing endogenous p62 localization and indicated bacterial strains. Scale bar, 1  $\mu$ m. (B) Percentage of indicated bacteria in A showing p62 localization. Data are mean  $\pm$  SD of three independent experiments ( $\geq 4$  FOV with  $\geq 200$  bacteria quantified per condition per independent experiment). (C) Western blot analysis of ATG5 expression in HeLa cell lysates from D. GAPDH, loading control. (D) Percentage of WT or *ATG5*<sup>-/-</sup> HeLa cells displaying BERCS with *sca2::Tn* mutant bacteria (48 hpi). The mean  $\pm$  SEM of three independent experiments (large outlined circles) are superimposed over the raw data the percent of cells with BERCS per FOV (small unlined circles) ( $>75$  cells quantified per condition per independent experiment) (one-way ANOVA with Dunnett's post hoc test). (E) Live-cell imaging snapshots at 28 hpi of *ompB::Tn* mutant (magenta) infecting A549-mCherry-Sec61 $\beta$  cells (cyan). Scale bar, 5  $\mu$ m; inset scale bar, 1  $\mu$ m. (F) Percentage of RpBFP or *ompB::Tn* mutant bacteria forming vacuole-like ER structures. RpBFP data are independent from that shown in Figs. 1 and 2. Each dot represents the mean percentage of bacteria interacting with the ER for three independent experiments ( $>500$  bacteria per independent experiment). Error bars represent SEM. Source data are available for this figure: SourceData FS2.



**Figure S3. Reduced VAPA and VAPB expression does not alter intracellular bacterial burdens, and overexpressed full-length VAP proteins localize throughout the ER. (A)** Number of bacteria in cells infected with *sca2::Tn* mutant bacteria (28 hpi) after the indicated siRNA treatment. The mean  $\pm$  SEM of three independent experiments (large outlined circles) are superimposed over the raw data from individual cells (small unlined circles) (>25 cells counted per condition per independent experiment). **(B)** Number of bacteria in WT or VAPA/B DKO HeLa cells infected with *sca2::Tn* mutant bacteria (28 hpi). The mean  $\pm$  SEM of three independent experiments (large outlined circles) is superimposed over the raw data from individual cells (small unlined circles) (>25 cells counted per condition per independent experiment). **(C and D)** Live-cell imaging snapshots at 28 hpi of *sca2::Tn* mutant (magenta) infecting A549-mCherry-Sec61β cells (cyan) transiently expressing HaloTag-VAPA (A) or HaloTag-VAPB (yellow) (B). Scale bar, 5  $\mu$ m; inset, 2.5  $\mu$ m.

**Video 1. *R. parkeri* forms stable interactions with the ER** A549-mCh-Sec61β cells (cyan) infected with RbFPF (magenta) for 28 h show stable vacuole-like ER structures around the bacterium (arrow) (see also Fig. 1 F). A single z slice is shown, and frames were captured every 20 s. Timestamp shows seconds (s). Scale bar, 2.5  $\mu$ m. Playback speed is 1x.

Video 2. **Formation of a vacuole-like ER interaction around *R. parkeri* A549-BiP-mNeonGreen-KDEL cells (cyan) infected with RpBFP (magenta) for 28 h showing the formation of a vacuole-like ER structure around a bacterium (arrow).** A single z slice is shown, and frames were captured every 20 s. Timestamp shows seconds (s). Scale bar, 2.5  $\mu\text{m}$ . Playback speed is 1 $\times$ .

Video 3. **The *sca2::Tn* mutant forms long-lived interactions with the ER A549-mCh-Sec61 $\beta$  cells (cyan) infected with the *sca2::Tn* mutant (magenta) for 24 h show very stable vacuole-like ER structures around the bacterium.** A single z slice is shown, and frames were captured every 5 min. Timestamp shows minutes (min). Scale bar, 2.5  $\mu\text{m}$ . Playback speed is 1 $\times$ .

Video 4. **Segmentation of *R. parkeri*-associated ER membranes during infection.** A549 cells infected with the *sca2::Tn* mutant for 30 h were imaged using FIB-SEM (data from Fig. 4). The initial frame shows a subregion of the FIB-SEM image stack followed by vertical slicing. Then, segmentation results showing the ER (cyan) and bacteria (magenta) appear on the FIB-SEM image stack, followed by vertical slicing to reveal the segmentation of both structures on each image slice. Playback speed is 1 $\times$ .

Video 5. ***R. parkeri*-associated ER membranes are connected to the greater ER network.** The initial frame shows the subregions shown in Video 4 followed by vertical slicing to reveal the 3D-rendered ER (cyan) and bacteria (magenta). Horizontal slicing of the ER network follows to highlight the connection between the rickettsia-associated ER and the greater ER network. Playback speed is 1 $\times$ .